# Ultrahigh B doping ($\leqslant 10^{22}$ $cm^{-3}$) during Si(001) gas-source molecular-beam epitaxy: B incorporation, electrical activation, and hole transport

G. Glass, H. Kim, P. Desjardins, N. Taylor, T. Spila, Q. Lu, and J. E. Greene
*Materials Science Department, The Coordinated Science Laboratory, and The Materials Research Laboratory, University of Illinois, 1101 West Springfield, Urbana, Illinois 61801*

(Received 28 June 1999)

Si(001) layers doped with B concentrations $C_B$ between $1\times10^{17}$ and $1.2\times10^{22}$ $cm^{-3}$ (24 at %) were grown on Si(001)2×1 at temperatures $T_s = 500$–$850\,°C$ by gas-source molecular-beam epitaxy from $Si_2H_6$ and $B_2H_6$. $C_B$ increases linearly with the incident precursor flux ratio $J_{B_2H_6}/J_{Si_2H_6}$ and B is incorporated into substitutional electrically active sites at concentrations up to $C_B^*(T_s)$ which, for $T_s = 600\,°C$, is $2.5\times10^{20}$ $cm^{-3}$. At higher B concentrations, $C_B$ increases faster than $J_{B_2H_6}/J_{Si_2H_6}$ and there is a large and discontinuous decrease in the activated fraction of incorporated B. However, the total activated B concentration continues to increase and reaches a value of $N_B = 1.3\times10^{21}$ $cm^{-3}$ with $C_B = 1.2\times10^{22}$ $cm^{-3}$. High-resolution x-ray diffraction (HR-XRD) and reciprocal space mapping measurements show that all films, irrespective of $C_B$ and $T_s$, are fully strained. No B precipitates or misfit dislocations were detected by HR-XRD or transmission electron microscopy. The lattice constant in the film growth direction $a_\perp$ decreases linearly with increasing $C_B$ up to the limit of full electrical activation and continues to decrease, but nonlinearly, with $C_B > C_B^*$. Room-temperature resistivity and conductivity mobility values are in good agreement with theoretical values for B concentrations up to $C_B = 2.5\times10^{20}$ and $2\times10^{21}$ $cm^{-3}$, respectively. All results can be explained on the basis of a model which accounts for strong B surface segregation to the second-layer with a saturation coverage $\theta_{B,sat}$ of 0.5 ML (corresponding to $C_B = C_B^*$). At higher $C_B$ (i.e., $\theta_B > \theta_{B,sat}$), B accumulates in the upper layer as shown by thermally programmed desorption measurements, and a parallel incorporation channel becomes available in which B is incorporated into substitutional sites as B pairs that are electrically inactive but have a low charge-scattering cross section.

## I. INTRODUCTION

Ultrahigh B doping (concentrations $C_B > 5\times10^{19}$ $cm^{-3}$) in Si is currently of interest for use as emitter layers in Si bipolar transistors,[1] base layers in $Si/Si_{1-x}Ge_x$ heterostructure bipolar transistors,[2] source and drain regions in metal-oxide semiconductor transistors, electromigration-resistant selectively-grown epitaxial zero-level metallization layers,[3,4] and etch stop layers.[5] Reported B equilibrium solid solubilities in Si range from $8\times10^{20}$ $cm^{-3}$ at 1400 °C (Ref. 6) to $\simeq 1$–$1.5\times10^{20}$ $cm^{-3}$ at 1000 °C (Refs. 7 and 8) and $2\times10^{19}$ $cm^{-3}$ at 700 °C.[7] Electrically active B concentrations of $1$–$3\times10^{20}$ $cm^{-3}$ have been reported for Si(001): B layers grown by ultrahigh vacuum chemical-vapor deposition[9] and solid-source molecular-beam epitaxy.[10] However, the reaction paths leading to the incorporation of both electrically active as well as inactive B are not understood.

B has been the primary $p$-type dopant in Si device fabrication for more than 30 years, yet there is still no consensus on the mechanism leading to B deactivation at high concentrations. Reports of B precipitates observed in transmission electron microscopy (TEM) images from ion-implanted Si (Ref. 11) with $C_B > 1\times10^{17}$ $cm^{-3}$ were later shown to be incorrect. The features were actually dislocation loops, as determined by $\bar{g}\cdot\bar{b}$ analyses of TEM images (where $\bar{g}$ is the diffraction vector and $\bar{b}$ is the dislocation Burgers's vector).[12] The loops form as Si self-interstitials, created during implantation, condense during post-implant annealing to yield regions with inserted {113} planes.[13] Similar structures have been observed, following annealing at 900 °C for 100 h, in B-doped Czochralski-grown Si with $C_B = 1\times10^{19}$ $cm^{-3}$.[14] In this case, the thermally generated Si self interstitials condense on {112} planes. Electrical deactivation of B acceptors has been reported to be linked to the presence of the above dislocation structures.[13]

Here, we present direct evidence for B deactivation in defect-free (as judged by TEM and high-resolution x-ray diffraction) Si(001) films. This implies that the complex responsible for B deactivation is of size ≲50 Å. Previously proposed nanoscale clustering mechanisms include B pairs,[15] two types of $B_{12}$ clusters,[16] and amorphous B clusters.[17] Newman and Smith[15] found three infrared peaks, corresponding to absorption from $^{11}B$-$^{11}B$, $^{11}B$-$^{10}B$, and $^{10}B$-$^{10}B$ pairs, in Czochralski-grown B-doped Si with $C_B = 5\times10^{19}$ $cm^{-3}$. The relative peak amplitudes matched B isotopic abundances. An *ab initio* pseudopotential calculation, using a 64-atom supercell, predicted that the lowest-energy configuration for B clusters in Si corresponds to B pairs aligned along ⟨001⟩ directions, occupying single Si sites, and having a bond length of 1.6 Å.[18]

Our group has previously demonstrated[19] that for B concentrations up to $2\times10^{19}$ $cm^{-3}$ in Si(001) layers grown by gas-source molecular-beam epitaxy (GS-MBE) from $B_2H_6/Si_2H_6$ mixtures, $C_B$ increases linearly with increasing flux ratio $J_{B_2H_6}/J_{Si_2H_6}$ at constant film growth temperature $T_s$ (600–950 °C) and decreases exponentially with $1/T_s$ at constant $J_{B_2H_6}/J_{Si_2H_6}$ ($9.3\times10^{-5}$–$2.5\times10^{-2}$). B incorporation

0163-1829/2000/61(11)/7628(17)/$15.00  ©2000 The American Physical Society

is thermally activated and $B_2H_6$ reactive sticking probabilities range from $\simeq 6.4\times10^{-4}$ at $T_s=600\,°C$ to $1.4\times10^{-3}$ at 950 °C (Ref. 19) while Si deposition from $Si_2H_6$ is precursor mediated.[20] Temperature-dependent (20–300 K) hole carrier mobilities are equal to the best reported bulk Si:B data and are in good agreement with theoretical maximum values. Over the range in doping concentrations investigated, $C_B = 5\times10^{16}-2\times10^{19}$ cm$^{-3}$, the presence of B had no significant effect on film growth rates, $R_{Si}$.

We have recently shown that higher B doping during Si(001) GS-MBE from $B_2H_6/Si_2H_6$ mixtures leads to complex and competing kinetic effects giving rise to an increase in film growth rates $R_{Si}$ by $\gtrsim$50% with increasing $C_B \gtrsim 1\times10^{19}$ cm$^{-3}$ at film growth temperatures $T_s \leqslant 550\,°C$ and a decrease by corresponding amounts at $T_s \geqslant 600\,°C$.[21–23] At low film growth temperatures where steady-state $H$ coverages $\theta_H$ are large, $R_{Si}$ increases due to strong B surface segregation (with enthalpy $\Delta H_s = -0.53$ eV) (Ref. 23) to the second layer. This enhances H-desorption rates, primarily through backbond charge transfer from surface Si-H bonds to B-Si backbonds. At high $T_s$, $\theta_H$ is small and the primary effect of high-B coverages is to deactivate surface dangling bonds and, hence, to decrease the density of reactive sites. Hydrogen binding energies and dangling bond coverages as a function of $C_B$, $\theta_B$, and $T_s$ were quantitatively determined by isotopically tagged $D_2$ temperature programmed desorption (TPD). The data were then used to model $R_{Si}(C_B, T_s)$ with no fitting parameters. The results are in very good agreement with measured growth rate data.[23]

In this paper, we present the results of an investigation of ultrahigh B dopant incorporation and electrical activation during Si(001):B GS-MBE. The films were grown from $Si_2H_6$ and $B_2H_6$ as a function of temperature ($T_s = 500-850\,°C$) and incident $B_2H_6$ flux ($J_{B_2H_6} = 7.0\times10^{12}-6.6\times10^{16}$ cm$^{-2}$ s$^{-1}$) with $J_{Si_2H_6}$ maintained constant at $2.2\times10^{16}$ cm$^{-2}$ s$^{-1}$. All B was incorporated into substitutional electrically active sites for $C_B \leqslant 2.5\times10^{20}$ cm$^{-3}$ ($T_s = 600\,°C$), corresponding to a saturation B second-layer coverage $\theta_B$ of 0.5 ML. At higher $C_B$, $\theta_B$ exceeds 0.5 ML and an additional B incorporation mechanism becomes operative allowing incorporation of B pairs at substitutional Si sites. The latter are not electrically active but have low charge-scattering cross sections and thus relatively little effect on carrier mobilities.

All films were fully strained with no indication by high-resolution x-ray diffraction (HR-XRD), high-resolution reciprocal-space lattice mapping, or HR-TEM of misfit dislocations or B precipitates. The film lattice constant along the growth direction $a_\perp$ decreases linearly with increasing substitutional B concentration and increases linearly, although at a much lower rate, with increasing B-pair concentration. Room-temperature hole conductivity mobilities $\mu_h$ range from 170 to 48 cm$^2$ V$^{-1}$ s$^{-1}$ for hole concentrations of $p = C_B = 1\times10^{17}$ and $2.5\times10^{20}$ cm$^{-3}$. Even with $p = 4.0\times10^{20}$ cm$^{-3}$ ($C_B = 1.3\times10^{21}$ cm$^{-3}$), $\mu_h$ remains relatively high at 41 cm$^2$ V$^{-1}$ s$^{-1}$. The metal-insulator transition at room temperature occurs at a B concentration of approximately $8\times10^{18}$ cm$^{-3}$ and the minimum resistivity is 300 $\mu\Omega$ cm.

## II. EXPERIMENTAL PROCEDURE

The films were grown in a multichamber ultrahigh vacuum system, described in detail in Refs. 19 and 20. The system is evacuated using a combination of ion and turbomolecular pumps to provide a base pressure of $\simeq 5\times10^{-11}$ Torr. The growth chamber, equipped with reflection high-energy electron diffraction (RHEED) and a quadrupole mass spectrometer (QMS), is connected through a transfer chamber to an analytical station containing provisions for Auger electron spectroscopy (AES), electron energy loss spectroscopy, and low-energy electron diffraction (LEED). TPD measurements are performed in a chamber attached to the analytical station, containing a heavily differentially pumped Extrel QMS.

B-doped Si(001) layers, 0.12–2.0 $\mu$m thick, were grown from $Si_2H_6$ and $B_2H_6$ molecular beams delivered to the substrate through individual directed tubular dosers located 3 cm from the substrate at an angle of 45°. The dosers are coupled to feedback-controlled constant-pressure reservoirs in which pressures are separately monitored using capacitance manometers whose signals are in turn used to control variable leak valves. Valve sequencing, pressures, gas flows, and substrate temperature are all computer controlled.

The Si(001) substrates were $1\times3$ cm$^2$ plates cleaved from 0.5-mm-thick $n$-type (resistivity=23–28 $\Omega$ cm, $n = 1-2\times10^{14}$ cm$^{-3}$) wafers. Initial cleaning consisted of degreasing by successive rinses in warm trichloroethane, acetone, propanol, and deionized water. The substrates were then subjected to four wet-chemical oxidation/etch cycles consisting of the following steps: 2 min in a 2:1:1 solution of $H_2O$:HCl:$H_2O_2$, rinse in fresh deionized water, and a 30-s etch in dilute (10%) HF. They were blown dry with ultrahigh purity $N_2$, exposed to a UV/ozone treatment which consists of UV irradiation from a low-pressure Hg lamp (15 mW cm$^{-2}$) for 30 min in air to remove C-containing species,[24] and introduced into the deposition system through the transfer chamber. There, they were degassed at 600 °C for 4 h, cooled to 200 °C, and then rapidly heated at $\simeq 100\,°C\,s^{-1}$ to 1100 °C for 1 min to remove the oxide. The pressure increase during oxide desorption was $\leqslant 3\times10^{-9}$ Torr for a duration of less than 10 s.

Substrates processed using the above procedure exhibited $2\times1$ RHEED patterns consisting of well-defined diffraction spots, rather than streaks, with sharp Kikuchi lines and essentially equi-intense fundamental and half-order reflections. The layer surfaces were thus atomically smooth with relatively large terraces. No C or O was detected by *in situ* AES. Substrate temperatures were determined using Pt-Rh thermocouples calibrated by optical pyrometry.

Undoped Si buffer layers, 200 Å thick for Hall-effect samples and 6000 Å for all others, were grown at 800 °C prior to commencing Si:B film growth. The buffer layers serve two purposes. They cover any remaining surface contamination while simultaneously providing a more uniform distribution of terrace lengths.[25] The primary Si(001):B film growth temperatures were $T_s = 550$ and 600 °C in the surface-reaction-limited growth regime, but films were also grown at 500 °C and in the flux-limited growth mode at 700, 800, and 850 °C in order to investigate the effect of ultrahigh B doping on $R_{Si}$ as a function of $T_s$. The incident disilane

flux was $J_{Si_2H_6} = 2.2 \times 10^{16}$ cm$^{-2}$ s$^{-1}$ while the diborane flux $J_{B_2H_6}$ was varied from $7.0 \times 10^{12}$ to $6.6 \times 10^{16}$ cm$^{-2}$ s$^{-1}$.

TPD measurements were carried out *in situ*. Following Si(001):B growth, the films were quenched to <200 °C and exposed to atomic deuterium until saturation coverage. For this purpose, $D_2$ was delivered through a doser identical to those described above, but with a hot W filament near the outlet to crack the gas. All H was exchanged for D as demonstrated by TPD. The TPD experiments themselves have no measurable effect on B surface segregation, as shown by the fact that the ratio of the B (*KLL* 179 eV) to Si(*LMM* 92 eV) AES peak intensities remain constant, and successive TPD measurements yield identical results. For TPD analyses, samples were heated at a linear rate of 2 °C s$^{-1}$. The experiments were performed with the sample 2 mm from the 5-mm diameter hole in the skimmer cone of a heavily differentially pumped Extrel QMS. Deuterium was employed rather than hydrogen in order to suppress the background signal.

Deposited film thicknesses were measured using microstylus profilometry while B concentrations in as-deposited layers were determined using a Cameca IMS-5E secondary ion mass spectrometer (SIMS) operated with a 10 keV $O_2^+$ primary ion beam to detect $^{11}$B. Quantification, with an experimental uncertainty of ±10%, was accomplished by comparison to B ion-implanted bulk Si(001) standards. Other than intentionally introduced B, the films contained no detectable impurities.

High-resolution x-ray diffraction (HR-XRD) measurements were performed using a four-axis diffractometer with a collimating x-ray mirror, a Bartels four-crystal Ge(022) monochromator, and an Euler sample cradle with independent computer-controlled drive of all sample rotation angles. The instrument is capable of positioning samples to within 1 arc s. Cu $K\alpha_1$ radiation ($\lambda = 1.540\,597$ Å) with angular divergence <12 arc s and a wavelength spread of $\simeq 2 \times 10^{-5}$ was incident at an angle $\omega$ with respect to the sample surface. Overview $\omega$-$2\theta$ scans ($\theta$ is the diffraction angle) were performed using a wide-aperture ($\simeq 2°$) detector with a rotation rate twice that of the sample. In order to investigate the orientation dependence of x-ray scattering distributions from the films, the detector acceptance was reduced to ≃12 arc s by placing a three-reflection Ge crystal analyzer between the sample and the detector. High-resolution reciprocal space maps were then constructed from successive $\omega$-$2\theta$ scans, centered at different values of $\omega$. Recorded intensities are plotted as two-dimensional topographical contour maps as a function of wave vector perpendicular $k_\perp$ and parallel $k_\parallel$ to the surface.

Resistivity and Hall-effect measurements were carried out as a function of temperature between 25 and 300 K. Samples were measured in the van der Pauw configuration[26] with ohmic contacts formed by evaporating Al through a mask and annealing the sample in high vacuum at 300 °C for 60 s. In-clad Pt electrical leads were soldered to the Al contacts. The magnetic field strength for the Hall measurements was 10 kG. Lightly doped *n*-type substrates ($n = 1 \times 10^{14}$ cm$^{-3}$) were used in order to create a large depletion layer which extends deep (3–3.5 $\mu$m) into the substrate while being of negligible width (<30 Å) in all films in this study ($p = 10^{17}-10^{22}$ cm$^{-3}$) due to the large difference in doping levels.[27] The depletion region electrically isolates the substrate from the film during measurement. The minimum film thickness for Hall effect samples was 5000 Å.

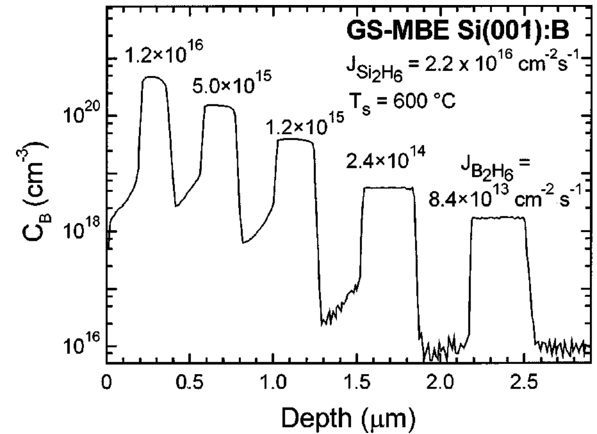


FIG. 1. SIMS depth profiles through a B modulation-doped Si(001):B film grown by GS-MBE from $Si_2H_6$ and $B_2H_6$ at $T_s = 600$ °C. The incident $Si_2H_6$ flux was $J_{Si_2H_6} = 2.2 \times 10^{16}$ cm$^{-2}$ s$^{-1}$ while the B flux $J_{B_2H_6}$ was varied from $8.4 \times 10^{13}$ to $1.2 \times 10^{16}$ cm$^{-2}$ s$^{-1}$. The deposition time for each layer was constant at 1 h.

Cross-sectional transmission electron microscopy (XTEM) examinations were performed in a Philips CM12 microscope operated at 120 kV while high-resolution lattice images were obtained at 300 kV using an Hitachi H9000 microscope. XTEM samples were scribed and cleaved into $2 \times 4$ mm$^2$ pieces, which were glued film to film and then cut with a diamond saw into $2 \times 1.5$ mm slabs approximately 0.4 mm thick. The samples were then glued to Pyrex glass plates and polished from both sides with 500 grit SiC paper then with 0.3 $\mu$m alumina polishing wheels to reduce the total thickness to 20–25 $\mu$m. Final thinning to electron transparency was achieved by $Ar^+$ ion milling from both sides. The incident beam angle and energy were progressively reduced from 15° to 11° and 5 to 3.5 keV in order to minimize radiation damage artifacts and to obtain samples with relatively even thickness distributions. The samples were cooled during ion milling such that their temperature never exceeded 100 °C.

## III. RESULTS

### A. Boron incorporation

More than 70 single-layer and multilayer B-doped Si(001) films were grown in order to determine B incorporation probabilities as a function of $J_{B_2H_6}/J_{Si_2H_6}$ and $T_s$. A typical SIMS profile through a B modulation-doped sample is presented in Fig. 1 for a Si(001) multilayer film grown at $T_s = 600$ °C with successive B-doped regions separated by undoped buffer layers. The deposition time for all layers was 60 min with $J_{Si_2H_6}$ maintained constant at $2.2 \times 10^{16}$ cm$^{-2}$ s$^{-1}$ while $J_{B_2H_6}$ was varied to provide $C_B$ values from $1.7 \times 10^{18}$ to $4.7 \times 10^{20}$ cm$^{-3}$. SIMS results from layers with $C_B \lesssim 2 \times 10^{18}$ cm$^{-3}$ exhibit no measurable B segregation and yield profiles which are essentially flat with the leading and trailing edges abrupt to within experimental resolution, 80 Å

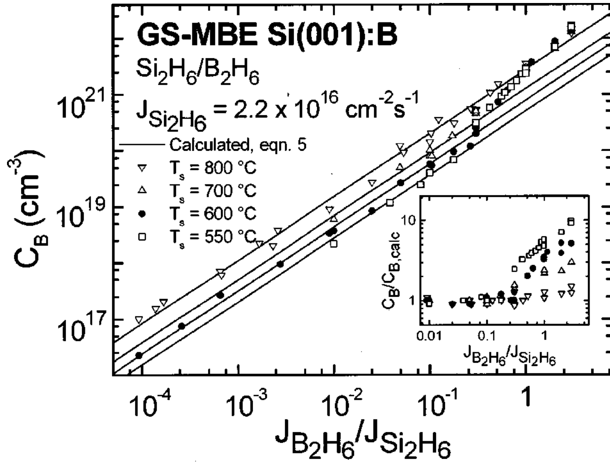


FIG. 2. Incorporated B concentrations $C_B$ in GS-MBE Si(001) layers as a function of the incident flux ratio $J_{B_2H_6}/J_{Si_2H_6}$ during growth at temperatures $T_s$ of 550, 600, 700, and 800 °C. The inset shows the ratio of measured (SIMS) to calculated [Eq. (5)] B concentration $C_B$ as a function of $J_{B_2H_6}/J_{Si_2H_6}$.

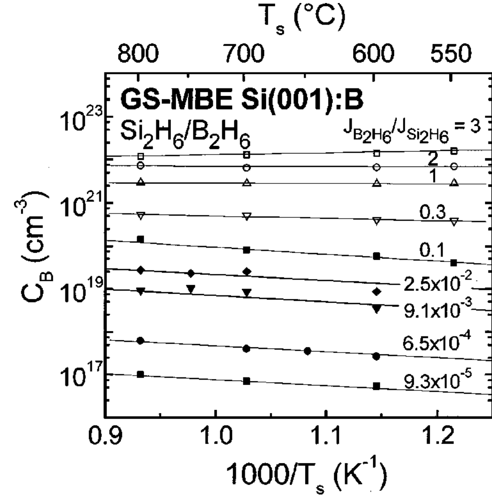


FIG. 3. Incorporated B concentrations $C_B$ in GS-MBE Si(001) layers as a function of the growth temperature $T_s$ with incident flux ratios $J_{B_2H_6}/J_{Si_2H_6}$ maintained constant at values between $9.3\times10^{-5}$ and 3.0.

per concentration decade. Significant B segregation is observed, however, in layers deposited under conditions corresponding to higher steady-state B concentrations. With $C_B \gtrsim 2\times10^{18}$ cm$^{-3}$, the B incorporation probability is initially depressed giving rise to SIMS profiles with ''missing'' B at the back side as B accumulates at the surface until a steady-state surface-to-bulk B fraction ratio $r_B$ is achieved. The value of $r_B$ depends upon $T_s$, $R_{Si}$, and $J_{B_2H_6}$. After turning off the $B_2H_6$ flux, the excess B at the surface acts as a reservoir, in multilayer samples, to continue doping what was intended to be undoped buffer layers.

A comparison of the widths of the profiles in Fig. 1 clearly shows, in agreement with the results in Refs. 22 and 23, that the Si deposition rate at 600 °C decreases with increasing $C_B$ at high $J_{B_2H_6}/J_{Si_2H_6}$ ratios. B doping at concentrations greater than $\simeq 5\times10^{20}$ cm$^{-3}$ induces surface roughness which propagates in multilayer samples, thus introducing error in the SIMS depth resolution. Therefore, layer thicknesses used for growth rate determinations in samples with high-$C_B$ values were obtained from single-layer films in order to minimize the number of interfaces.

At constant $T_s$ and $J_{Si_2H_6}$, the total incorporated B concentration $C_B$, as measured by SIMS, increases linearly with the flux ratio $J_{B_2H_6}/J_{Si_2H_6}$ up to $\simeq 0.25$ ($J_{B_2H_6} = 5.5\times10^{15}$ cm$^{-2}$ s$^{-1}$) as shown in Fig. 2 for layers grown at $T_s = 550$, 600, 700, and 800 °C. At $T_s = 600$ °C, for example, Fig. 2 shows that $J_{B_2H_6}/J_{Si_2H_6} = 0.25$ corresponds to $C_B = 2.5\times10^{20}$ cm$^{-3}$. The solid lines in Fig. 2 were calculated using the procedure outlined in Sec. IV B and agree well with experimental $C_B(J_{B_2H_6}/J_{Si_2H_6}, T_s)$ data throughout the linear B incorporation range at all growth temperatures. However, as $J_{B_2H_6}/J_{Si_2H_6}$ becomes greater than $\simeq 0.3$, measured B concentrations exceed calculated values by amounts that increase with the flux ratio and are larger at lower temperatures for a given value of $J_{B_2H_6}/J_{Si_2H_6}$. The inset in Fig. 2 shows that the ratio of measured to calculated B concentrations, $C_B/C_{B,calc}$, increases with decreasing $T_s$ yielding $C_B/C_{B,calc}$ values as high as 10 with $J_{B_2H_6}/J_{Si_2H_6} = 3$ and $T_s = 550$ °C.

Figure 3 is a plot of $C_B$ as a function of $T_s$ for incident flux ratios $J_{B_2H_6}/J_{Si_2H_6}$ between $9\times10^{-5}$ and 3. With $J_{B_2H_6}/J_{Si_2H_6} \leqslant 0.1$, the slope of $\ln(C_B)$ vs $1/T_s$ remains constant and negative corresponding to a positive activation energy, the signature of a thermally activated process,[19] for B chemisorption. At higher $J_{B_2H_6}/J_{Si_2H_6}$ ratios, the slope continuously increases and becomes positive with $J_{B_2H_6}/J_{Si_2H_6} > 2$. The change in slope signifies that additional surface reaction paths leading to B incorporation become active. The trend toward a more positive slope at higher $J_{B_2H_6}/J_{Si_2H_6}$ values indicates that an additional B incorporation pathway at high-B concentrations has a negative activation energy and, hence, is precursor mediated.

### B. Hole concentrations

Effective hole concentrations $p_e$ in B-doped Si(001) films grown at $T_s = 600$ °C with total B concentrations $C_B = 1\times10^{17}$–$1.2\times10^{22}$ cm$^{-3}$ were determined from temperature-dependent (25–300 K) Hall-effect measurements using the following relationship:[6]

$$p_e = \frac{\gamma}{qR_H}, \tag{1}$$

in which $q$ is the elementary charge, $R_H$ is the Hall coefficient, and $\gamma$ is the Hall scattering factor defined as the ratio of the Hall mobility to the conductivity mobility. We use an ''effective'' hole concentration in Eq. (1) since, as we show below, there is a range in B concentrations over which measured $p_e$ values are larger than the corresponding valence-band hole concentrations, primarily due to changes in the density of states (DOS), which decrease the band gap and give rise to higher effective intrinsic carrier concentrations.[28]

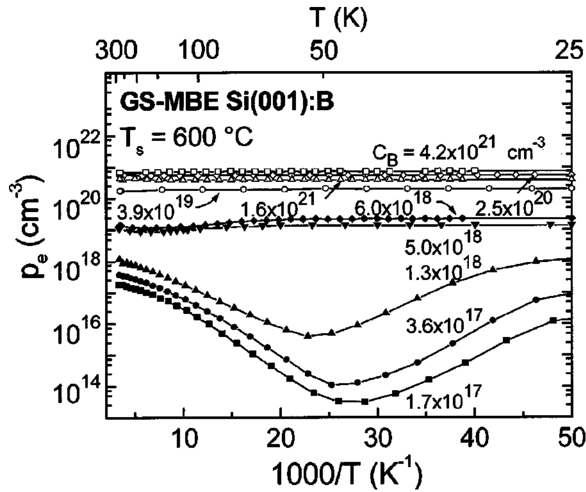


FIG. 4. Representative data sets showing the effective hole concentration $p_e$ as a function of temperature $T$ for B-doped GS-MBE Si(001) layers grown from $Si_2H_6/B_2H_6$ mixtures at $T_s = 600\,°C$. $C_B$ is the total incorporated B concentration.

A convenient treatment of hole transport assumes a scattering factor of unity, but this has been shown to result in an overestimate of the dopant concentration in $p$-type Si.[29–32] $\gamma$ was calculated by Lin *et al.*,[33] accounting for the nonparabolic and anisotropic nature of the valence band, to be 0.77 while Lu *et al.*[34] measured $\gamma$ as 0.75 for Si(001) B with $C_B = 5\times10^{16} - 1.3\times10^{18}$ cm$^{-3}$. We have used $\gamma = 0.75$ and assumed it to be independent of $C_B$, consistent with the reported weak functional dependence.[33,34]

Typical curves of $p_e$ vs reciprocal temperature are shown in Fig. 4 for samples with $C_B = 1.7\times10^{17}$–$1.2\times10^{22}$ cm$^{-3}$. All curves shift in a systematic manner with increasing $C_B$. For clarity, data are plotted from only nine samples in order to illustrate the primary trends. A data set listing $p_e$ values for all samples at 77, 150, and 300 K is given in Table I.

Three distinct carrier regimes are visible in Fig. 4: the itinerant-hole semiconductor regime at low $C_B$, the metallic regime at high $C_B$, and an intermediate mixed-conductivity mode. Near room temperature, the curves from the three lowest doped samples in Fig. 4 ($C_B = 1.7$, 3.6, and $13\times10^{17}$ cm$^{-3}$) are in the exhaustion region in which all acceptor states are ionized and $p_e \simeq N_B$. In the carrier-freeze-out region at temperatures between $\simeq 175$ and 75 K, $p_e$ initially decreases with decreasing temperature with a slope equal to $-E_B/2k$ in which $E_B = 45$ meV (Ref. 6) is the B acceptor ionization energy in Si. With further sample cooling, $p_e$ reaches a minimum and then increases again due to hopping conduction through impurity states in the gap.[35] For samples with $C_B > 4\times10^{17}$ cm$^{-3}$, the slopes of the $p_e$ vs $1/T$ curves in the carrier freeze-out regime become progressively shallower with increasing $C_B$ showing that the energy required to excite holes from the acceptor states to the top of the valence band is decreasing. This, as described in more detail below, is primarily due to tailing in the valence band resulting from the increased hole density and the random spatial distribution of acceptors. The impurity states broaden as well, however this effect is negligible compared to valence-band tailing.[36]

Experimental $p_e$ vs $T$ curves for all films with $C_B < 4\times10^{17}$ cm$^{-3}$ were analyzed using the charge neutrality equation written for a single acceptor. The analysis accounted for valence-band spin-orbit splitting, included the full Fermi integral, and used an effective-mass valence-band DOS as in Ref. 19. Values of the electrically active B concentration $N_B$ and unintentional background donor concentrations $N_d$ were determined based upon nonlinear least-squares fits. The calculated curves exhibit very good agreement with the Hall-effect data. $N_B$ values were equal to $C_B$ within experimental uncertainty and $N_d$ for all samples was $< 9\times10^{13}$ cm$^{-3}$. Since all donors, irrespective of their ionization energy or origin (i.e., impurity or defect-related state) contribute to $N_d$, the maximum concentration of donorlike defects is $\leqslant 9\times10^{13}$ cm$^{-3}$. Similarly, the maximum concentration of shallow acceptorlike defects must also be $< 9\times10^{13}$ cm$^{-3}$.

The samples in Fig. 4 with $C_B = 5.0\times10^{18}$ and $6.0\times10^{18}$ cm$^{-3}$ have B concentrations near the metal-semiconductor transition. As the measurement temperature is reduced below 300 K, carrier freeze-out results first in about a 20% decrease in $p_e$ before hopping conduction begins to dominate and increase $p_e$ again until saturation is achieved at temperatures $\lesssim 60$ K. The combination of valence-band tailing (primarily) and broadening of the acceptor band formed by the overlap of acceptor-state wave functions eventually leads to overlap of the impurity and valence bands in films with $C_B \gtrsim 2\times10^{19}$ cm$^{-3}$. Thus, these samples do not exhibit carrier freeze out and are predominantly metallic in nature over the entire measurement temperature range.

In the intermediate conduction regime described above, prior to the onset of band overlap, increasing the acceptor-state hole density $p_{acc}$ (a function of both $C_B$ and $T$) eventually results in wave-function overlap becoming sufficiently large that direct tunneling, or hopping, of carriers between states is a significant component of the overall sample conductivity. Mott and co-workers[35,37,38] developed a straightforward prescription for characterizing the metal-semiconductor transition. The hydrogenic doping model,[6] accounting for the dielectric constant of the host material (Si, in this case) and the carrier effective mass, is used to estimate the Bohr radius and, hence, the volume ($\simeq 1.2\times10^5$ Å$^3$) ''occupied'' by holes bound to acceptors. The Mott transition is then defined to occur when $p_{acc}$ becomes sufficiently large that bound hole wave functions, whose spatial extent is defined by the above volume, just begin to overlap. Using Mott's criterion, acceptor state overlap becomes significant when $p_{acc} \gtrsim 8\times10^{18}$ cm$^{-3}$. This is consistent with our experimental results in Fig. 4 where samples with $C_B \geqslant 5\times10^{18}$ cm$^{-3}$ exhibit very little carrier freeze out. At even higher $C_B$, the valence-band tail advances into the gap sufficiently that it overlaps with the broadened impurity band.

As noted above, the acceptor ionization energy decreases with increasing $C_B$ for films with B concentrations greater than approximately $4\times10^{17}$ cm$^{-3}$. This should result in $p_e(300\text{ K}) \simeq N_B = C_B$, assuming complete electrical activation, within experimental uncertainty. The data in Fig. 4 and Table I show that it is indeed the case for layers with $C_B \lesssim 2\times10^{18}$ cm$^{-3}$. However, for films with higher B concentrations, $p_e(300\text{ K})$ values obtained from Hall-effect measurements vary significantly from $C_B$. That is, layers with $C_B$ between $2\times10^{18}$ and $5\times10^{20}$ cm$^{-3}$ have $p_e(300\text{ K})$

TABLE I. Effective hole concentrations $p_e$ and mobilities $\mu$ obtained from temperature-dependent Hall-effect measurements of GS-MBE Si(001):B layers grown at $T_s = 600\,°\mathrm{C}$ with B concentrations $C_{\mathrm{B}}$ ranging from $1.7\times 10^{17}$ to $1.2\times 10^{22}$ cm$^{-3}$.

| $C_{\mathrm{B}}$ (cm$^{-3}$) | $p_e$ (cm$^{-3}$) $T=77$ K | $p_e$ (cm$^{-3}$) $T=150$ K | $p_e$ (cm$^{-3}$) $T=300$ K | $\mu$ (cm$^2$ V$^{-1}$ s$^{-1}$) $T=77$ K | $\mu$ (cm$^2$ V$^{-1}$ s$^{-1}$) $T=150$ K | $\mu$ (cm$^2$ V$^{-1}$ s$^{-1}$) $T=300$ K |
|---|---|---|---|---|---|---|
| $1.7\times 10^{17}$ | $2.4\times 10^{15}$ | $7.0\times 10^{16}$ | $1.8\times 10^{17}$ | 1002 | 511 | 159 |
| $2.8\times 10^{17}$ | $2.0\times 10^{16}$ | $1.4\times 10^{17}$ | $2.9\times 10^{17}$ | 912 | 484 | 150 |
| $3.6\times 10^{17}$ | $7.7\times 10^{15}$ | $1.4\times 10^{17}$ | $3.7\times 10^{17}$ | 823 | 454 | 148 |
| $1.0\times 10^{18}$ | $2.5\times 10^{16}$ | $3.8\times 10^{17}$ | $1.0\times 10^{18}$ | 323 | 253 | 107 |
| $1.3\times 10^{18}$ | $3.0\times 10^{16}$ | $4.0\times 10^{17}$ | $1.2\times 10^{18}$ | 247 | 205 | 105 |
| $5.0\times 10^{18}$ | $1.2\times 10^{19}$ | $8.7\times 10^{18}$ | $1.1\times 10^{19}$ | 59 | 102 | 87 |
| $6.0\times 10^{18}$ | $1.7\times 10^{19}$ | $1.1\times 10^{19}$ | $1.4\times 10^{19}$ | 58 | 88 | 83 |
| $1.0\times 10^{19}$ | $3.1\times 10^{19}$ | $2.9\times 10^{19}$ | $3.0\times 10^{19}$ | 63 | 65 | 69 |
| $3.9\times 10^{19}$ | $1.9\times 10^{20}$ | $1.9\times 10^{20}$ | $1.7\times 10^{20}$ | 62 | 60 | 51 |
| $1.0\times 10^{20}$ | $3.5\times 10^{20}$ | $3.5\times 10^{20}$ | $3.5\times 10^{20}$ | 69 | 61 | 50 |
| $1.2\times 10^{20}$ | $3.7\times 10^{20}$ | $3.7\times 10^{20}$ | $3.7\times 10^{20}$ | 67 | 62 | 48 |
| $1.8\times 10^{20}$ | $4.6\times 10^{20}$ | $4.6\times 10^{20}$ | $4.6\times 10^{20}$ | 65 | 59 | 46 |
| $2.5\times 10^{20}$ | $5.5\times 10^{20}$ | $5.5\times 10^{20}$ | $5.5\times 10^{20}$ | 65 | 59 | 46 |
| $4.5\times 10^{20}$ | $5.6\times 10^{20}$ | $5.6\times 10^{20}$ | $5.6\times 10^{20}$ | 52 | 51 | 37 |
| $7.0\times 10^{20}$ | $3.0\times 10^{20}$ | $3.0\times 10^{20}$ | $3.0\times 10^{20}$ | 46 | 43 | 42 |
| $1.6\times 10^{21}$ | $4.8\times 10^{20}$ | $4.8\times 10^{20}$ | $4.8\times 10^{20}$ | 46 | 43 | 41 |
| $2.7\times 10^{21}$ | $6.5\times 10^{20}$ | $6.5\times 10^{20}$ | $6.5\times 10^{20}$ | 25 | 24 | 23 |
| $4.2\times 10^{21}$ | $7.8\times 10^{20}$ | $7.8\times 10^{20}$ | $7.8\times 10^{20}$ | 19 | 19 | 19 |
| $6.0\times 10^{21}$ | $9.0\times 10^{20}$ | $9.0\times 10^{20}$ | $9.0\times 10^{20}$ | 12 | 12 | 12 |
| $1.0\times 10^{22}$ | $1.2\times 10^{21}$ | $1.2\times 10^{21}$ | $1.2\times 10^{21}$ | 9 | 9 | 9 |
| $1.2\times 10^{22}$ | $1.3\times 10^{21}$ | $1.3\times 10^{21}$ | $1.3\times 10^{21}$ | 8 | 8 | 8 |

values which are actually larger than $C_{\mathrm{B}}$ by up to a factor of 4. Each B atom can only contribute a maximum of one hole to the valence band. The excess increase in carrier concentration results from increased thermal carrier generation due to band-gap narrowing and associated changes in the DOS when $C_{\mathrm{B}}$ exceeds $2\times 10^{18}$ cm$^{-3}$.[39]

Band-gap narrowing has been attributed to three primary causes:[36] fluctuations in the local lattice potential due to the random distribution of acceptors, electron-hole correlation, and hole-hole exchange effects. The first effect results in the largest contribution to band-gap narrowing and gives rise to band tailing with the introduction of new states in the gap while the latter two effects, listed in order of decreasing importance, produce rigid shifts in the band edges. As the DOS in the impurity band increases, the band also broadens. However, this contribution is small compared to band-edge tailing and can generally be ignored.[36] A quantum-mechanical description of band-edge tailing due to spatially dependent distortions in the local DOS developed by Lax and Philips[40] and Frisch and Lloyd[41] was used by Klauder[42] to derive an efficient computational algorithm to describe band-gap narrowing as a function of dopant concentration.

The electron-hole correlation energy arises from Coulomb screening of both the stationary acceptor ions and the minority carrier electrons while the hole-hole exchange energy results from the Pauli exclusion principle, which states that no two particles can have the same set of quantum numbers. The exclusion principle gives rise, in addition to an electrostatic repulsive energy, to repulsion between two holes of like spin. However, since the hole population has a random distribution of spin states, the overall repulsive energy decreases, which is equivalent to an attractive exchange energy. Electron-hole correlation effects shift the conduction-band edge down, while the hole-hole correlation effects decrease the acceptor level ionization energy. A theory describing changes in the band-gap energy due to hole-hole interactions and electron-hole correlations was originally derived by Mahan[43] and later confirmed by Sterne and Inkson.[44]

Bennett[39] developed a formalism based upon the work of Klauder[42] and Mahan[43] to quantitatively account for each of the above effects in determining the net shift in the valence- and conduction-band edges as well as the perturbed DOS and hence the effective intrinsic carrier concentrations, $n_{ie} \equiv p_{ie}$, as a function of doping density for both $n$- and $p$-type Si. We have applied Bennett's treatment to our experimental results in order to obtain the actual hole concentration $p$, and hence $N_B$, from the measured data. Calculated $p_{ie}$ values, normalized to the nondegenerate intrinsic carrier concentration $p_i$, initially increase with $C_{\mathrm{B}}$, due to band-gap narrowing, then decrease from a peak value of 4 at $C_{\mathrm{B}} = 7\times 10^{19}$ cm$^{-3}$ with increasing $C_{\mathrm{B}}$ as the valence-band tail begins to overlap with the B impurity band. When $C_{\mathrm{B}}$ exceeds $5\times 10^{20}$ cm$^{-3}$, essentially all transport is metallic and the measured carrier concentration is again equal to the ionized acceptor concentration. A calculated curve for $p_{ie}/p_i$, based upon Bennett's formalism, is plotted vs $C_{\mathrm{B}}$ in Fig. 5. The calculation was carried out between $8\times 10^{18}$ and $5\times 10^{20}$ cm$^{-3}$, due to the simplifications used in the model,[39] and the results extrapolated to $2\times 10^{18}$ cm$^{-3}$.

A comparison of our $C_{\mathrm{B}}$ values, determined by SIMS, with $p_e$, determined by Hall-effect measurements, shows

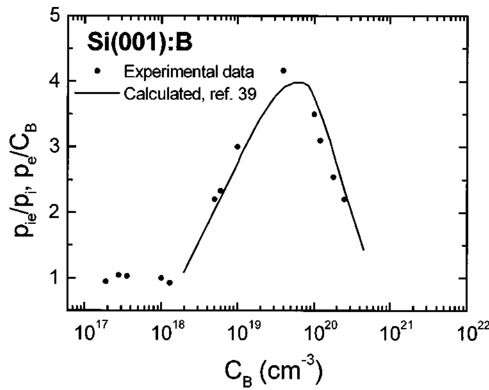


FIG. 5. Experimental data and calculated (solid line) ratio of the room-temperature effective hole concentration $p_e$ to the total incorporated B concentration $C_B$ plotted as a function of $C_B$. $p_{ie}$ and $p_i$ are the measured and non-degenerate hole concentrations, respectively. The solid line shows the theoretical curve derived in Ref. 39.

that $p_e > C_B$ over the B concentration between $5\times10^{18}$ and $\simeq 5\times10^{20}$ cm$^{-3}$ (see Table I). The ratio $p_e/C_B$ is plotted vs $C_B$ in Fig. 5 and shown to agree very well with Bennett's model.[39] We only plot data for $C_B \leq 2.5\times10^{20}$ cm$^{-3}$ for which we establish below, and in Sec. III E, that all B atoms are electrically active. Thus, although the effective carrier concentration is greater than $C_B$, the electrically active acceptor density $N_B$ remains equal to the B atom density $C_B$.

Figure 6 is a plot of $N_B$ vs $C_B$ over the entire B doping concentration range, spanning more than four decades, $C_B = 1\times10^{17}-1.2\times10^{22}$ cm$^{-3}$. The results show that B is incorporated into substitutional electrically active sites at concentrations up to $2.5\times10^{20}$ cm$^{-3}$. For samples with higher B concentrations, $N_B$ is increasingly less than $C_B$ as larger fractions of B are incorporated into electrically-inactive sites.

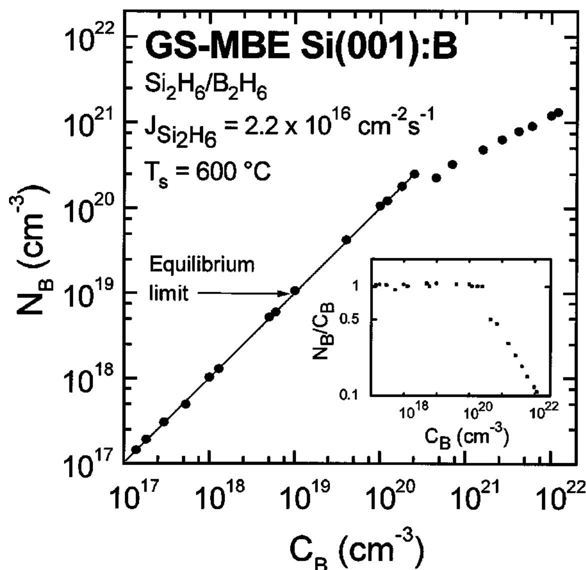


FIG. 6. B-acceptor concentrations $N_B$ determined from Hall-effect measurements vs the total incorporated B concentration $C_B$ obtained from SIMS analyses of GS-MBE Si(001) layers grown from $Si_2H_6/B_2H_6$ mixtures at $T_s = 600\,°C$. The inset shows the fraction $N_B/C_B$ of electrically active B as a function of $C_B$.

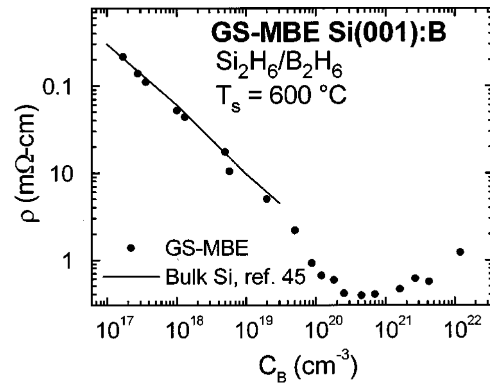


FIG. 7. Room-temperature resistivity $\rho$ as a function of B concentration $C_B$ in GS-MBE Si(001):B layers grown from $Si_2H_6/B_2H_6$ mixtures at $T_s = 600\,°C$. The solid line shows bulk Si data taken from Ref. 45.

Nevertheless, $N_B$ still continues to increase even up to the highest-doped sample with $C_B = 1.2\times10^{22}$ cm$^{-3}$ for which $N_B = 1.3\times10^{21}$ cm$^{-3}$.

### C. Resistivity

Figure 7 is a plot of room-temperature resistivity $\rho$ as a function of $C_B$ for GS-MBE Si(001):B. The results are equal to, or lower than, the best bulk Si:B data.[45] $\rho$ decreases with increasing $C_B$ to reach its lowest value $\rho_{\min} = 300\ \mu\Omega$ cm at $C_B = 2.5\times10^{20}$ cm$^{-3}$, remains approximately constant over a wide range in $C_B$, and then slowly increases again. As demonstrated in the above section, $C_B = 2.5\times10^{20}$ cm$^{-3}$ is the maximum B concentration at which 100% of the dopant atoms are electrically active.

The resistivity is inversely related to the carrier concentration and the mobility through the relation $\rho = (qp\mu)^{-1}$. The initial rapid decrease in $\rho(C_B)$ for $C_B \leq 2.5\times10^{20}$ cm$^{-3}$ is controlled primarily by the carrier concentration since, as we show below, the room-temperature carrier mobility changes relatively gradually with $C_B$ in this concentration range. However, as $C_B$ is raised above $2.5\times10^{20}$ cm$^{-3}$, an increasing fraction of the incorporated B is electrically inactive. Thus, $p$ increases much more slowly while $\mu$ continues to decrease with the net effect that $\rho(C_B)$ remains relatively constant over the $C_B$ range between $2.5\times10^{20}$ and $\simeq 2\times10^{21}$ cm$^{-3}$. This has the practical benefit that it provides a wide process window for fabrication of ultralow resistivity Si layers for use in high-power and/or current switching applications, local chip-level metallization, and active layers in bipolar and MOS transistors. Eventually, as $C_B > 2\times10^{21}$ cm$^{-3}$, $\rho$ increases as the local strain fields surrounding B atoms in the Si matrix begin to overlap and the atomic planes become sufficiently distorted to disrupt long-range order and give rise to incoherent carrier scattering.

Representative temperature-dependent resistivity data are shown in Fig. 8. The curve shapes continuously shift from those characteristic of semiconducting itinerant-hole valence-band conductivity at low-B concentrations to metallic conductivity at high-$C_B$ values. The initial decrease in the resistivity of layers with $C_B = 1.7$, 3.6, and $13\times10^{17}$ cm$^{-3}$ as a function of decreasing temperature is caused by a reduction

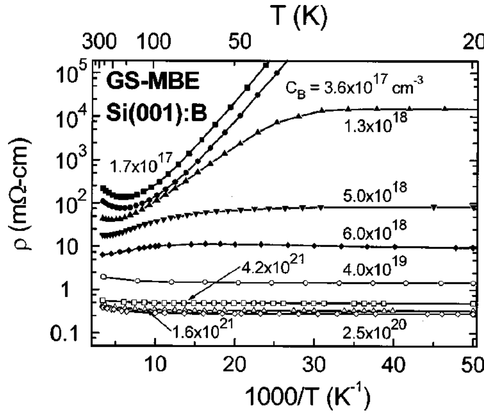


FIG. 8. Representative data sets showing the resistivity $\rho$ as a function of temperature $T$ for B-doped GS-MBE Si(001) layers grown from $Si_2H_6/B_2H_6$ mixtures at $T_s = 600\,°C$. $C_B$ is the total incorporated B concentration.

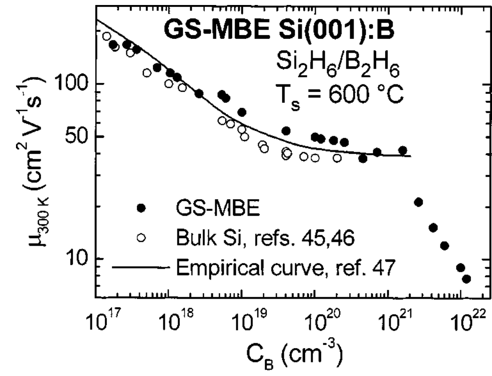


FIG. 9. Room-temperature hole mobility $\mu$ as a function of B concentration $C_B$ in Si:B. The filled circles are experimental data from GS-MBE Si(001):B layers grown from $Si_2H_6/B_2H_6$ mixtures at $T_s = 600\,°C$, the open circles are bulk Si data taken from Refs. 45 and 46, and the solid line is an empirical curve from Ref. 47.

in phonon scattering. However, $\rho$ increases again at temperatures below $\simeq 175$ K due primarily to a decrease in the hole concentration resulting from carrier freeze out. $\rho(T)$ curves for layers with $C_B = 5$ and $6\times10^{18}$ cm$^{-3}$, corresponding to the intermediate conduction regime, display a mixed-mode semiconducting plus hopping behavior. They are semiconductorlike in their temperature dependence near 300 K and metalliclike (i.e., no significant $T$ dependence) at low temperatures. Layers with $C_B \gtrsim 4\times10^{19}$ cm$^{-3}$ are predominantly metallic.

As $C_B$ approaches the metal-semiconductor transition, the low-temperature resistivity limit $\rho_0$ changes very rapidly. Figure 8 shows, for example, that $\rho_0$ decreases by more than two orders of magnitude as $C_B$ increases from $1.3\times10^{18}$ to $5\times10^{18}$ cm$^{-3}$. As discussed in the previous section, when the B concentration becomes high enough that the acceptor states begin to merge into an impurity band, the local DOS, and hence the sample conductivity, increases rapidly. The rapid rate of decrease in $\rho_0$ with $C_B$ is due to the fact that the state-to-state tunneling probability increases exponentially with decreasing tunneling distance. In the fully metallic regime, Fig. 8 shows, in agreement with Fig. 7, that as $C_B$ becomes larger than $2.5\times10^{20}$ cm$^{-3}$, $\rho$ increases with increasing $C_B$.

### D. Hole mobilities

Room-temperature hole conductivity mobilities $\mu$, derived from measured Hall mobilities using the relationship $\mu = \mu_H/\gamma$ with a Hall scattering factor $\gamma = 0.75$, are plotted in Fig. 9 as a function of B concentration. The conductivity mobility was used in order to directly compare the results with literature values for bulk Si:B. Figure 9 shows that the present mobilities are equal to, or greater, than the best bulk data[45,46] and are in good agreement with an empirical relationship (solid line) developed by Caughy and Thomas[48] and refined by Thurber *et al.*[47] $\mu$ ranges from 190 cm$^2$ V$^{-1}$ s$^{-1}$ with $C_B = 1.8\times10^{17}$ cm$^{-3}$ to 47 cm$^2$ V$^{-1}$ s$^{-1}$ with $C_B = 2.5\times10^{20}$ cm$^{-3}$, the limit of complete dopant electrical activity.

As B concentrations are increased above $2.5\times10^{20}$ cm$^{-3}$, corresponding to decreasing activated dopant fractions, $\mu$ remains approximately constant with $C_B$ up to $1.6\times10^{21}$ cm$^{-3}$ ($\mu = 41$ cm$^2$ V$^{-1}$ s$^{-1}$) for which the concentration of electrically inactive dopant atoms is $1.1\times10^{21}$ cm$^{-3}$. This indicates, as discussed further in Sec. IV C, that the scattering cross section of inactive B is small. At even higher B concentrations, however, the hole mobility decreases rapidly ($\mu = 8$ cm$^2$ V$^{-1}$ s$^{-1}$ with $C_B = 1.2\times10^{22}$ cm$^{-3}$).

Typical results for $\mu$ vs $T$ are plotted in Fig. 10 for representative layers with B concentrations ranging from $1.7\times10^{17}$ to $4.2\times10^{21}$ cm$^{-3}$. $\mu(T)$ data for the complete set of samples are listed in Table I. The curves in Fig. 10 for the three lowest doped layers, $C_B = 1.7$, 3.6, and $13\times10^{17}$ cm$^{-3}$, are in very good agreement with published curves for bulk $p$-type Si.[30,32] $\mu(T)$ initially increases with decreasing temperature following a negative power-law dependence. Over this temperature range, the mobility is primarily limited by phonon, ionized-impurity, and hole-hole scattering.[19] The power law exponent decreases with increasing carrier concentration due to increasing contributions from ionized-impurity and hole-hole scattering. As $T$ is decreased below 100–150 K, the negative slope of the $\mu$ vs $T$ curves decreases and eventually changes sign as hole carriers continue to freeze out and neutral impurity scattering dominates. Hole

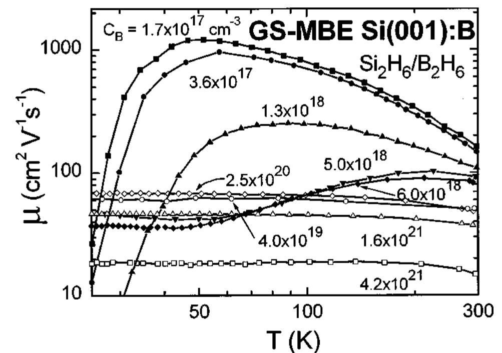


FIG. 10. Representative data sets showing the hole mobility $\mu$ as a function of temperature for B-doped GS-MBE Si(001) layers grown from $Si_2H_6/B_2H_6$ mixtures at $T_s = 600\,°C$. $C_B$ is the total incorporated B concentration.

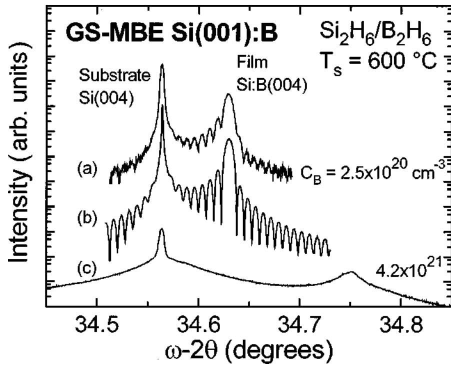


FIG. 11. High-resolution x-ray diffraction 004 $\omega$-$2\theta$ scans from: (a) a GS-MBE Si(001):B layer grown at $T_s = 600\,^\circ\mathrm{C}$ with a B concentration $C_B = 2.5\times10^{20}$ cm$^{-3}$; (b) a fully dynamical simulation assuming $C_B = 2.5\times10^{20}$ cm$^{-3}$, no strain relaxation, and perfectly uniform flat lattice planes; and (c) a GS-MBE Si(001):B layer grown at $T_s = 600\,^\circ\mathrm{C}$ with $C_B = 4.2\times10^{21}$ cm$^{-3}$.

mobilities at 77 K vary from 980 cm$^2$ V$^{-1}$ s$^{-1}$ with $C_B = 1.7\times10^{17}$ cm$^{-3}$ to 250 cm$^2$ V$^{-1}$ s$^{-1}$ with $C_B = 1.3\times10^{18}$ cm$^{-3}$.

At temperatures above 100 K, the two samples in Fig. 10 with B concentrations $C_B = 5\times10^{18}$ and $6\times10^{18}$ cm$^{-3}$, near the metal-semiconductor transition, exhibit $\mu(T)$ behavior which is qualitatively similar to that of the lower-doped samples. However, in this B concentration range, ionized-impurity scattering becomes more important and the transition from scattering dominated by phonons to impurity-dominated scattering shifts to higher temperatures. With further reduction in $T$, carrier mobilities decrease and then saturate below $\simeq 50$ K as impurity-band hopping conduction, which is only weakly temperature dependent, increasingly controls carrier transport.

Samples with $C_B$ above $4\times10^{19}$ cm$^{-3}$ appear completely metallic. Since the Fermi level is now well within the valence band, carrier freeze out is no longer observed and impurity scattering dominates at all temperatures. Thus, carrier mobilities for these layers exhibit little temperature dependence. 77 K hole mobilities in this dopant concentration range vary from 62 cm$^2$ V$^{-1}$ s$^{-1}$ with $C_B = 4\times10^{19}$ cm$^{-3}$ to 8 cm$^2$ V$^{-1}$ s$^{-1}$ with $C_B = 1.2\times10^{22}$ cm$^{-3}$.

### E. Film microstructure and strain

A combination of HR-XRD, reciprocal-lattice mapping, TEM, and XTEM was employed to examine the microstructure, crystalline quality, and strain-state of GS-MBE Si(001):B layers as a function of $C_B$. High-resolution reciprocal-lattice mapping is more sensitive than TEM to the initial stages of film relaxation through misfit dislocation generation. The resolution for detecting changes in film/substrate lattice-constant misfit in the present high-resolution mapping measurements is $\simeq 2\times10^{-5}$ corresponding to an average dislocation separation of 10 $\mu$m. In contrast, direct observation by TEM is limited to dislocation densities $\gtrsim 5\times10^3$ cm$^{-1}$ or changes in residual in-plane stress $\gtrsim 10^{-4}$. All films, even those with the highest-B concentrations, $C_B = 1.2\times10^{22}$ cm$^{-3}$, were found to be completely coherent with the substrate.

Figure 11(a) shows a typical overview 004 $\omega$-$2\theta$ scan, obtained with an open detector, of the Si substrate and Si:B layer. The film is 6500 Å thick with $C_B = 2.5\times10^{20}$ cm$^{-3}$ and was grown at 600 °C. Finite-thickness fringes, which arise due to interference of diffracted waves scattered from a finite number of lattice planes, are observed in the region between the substrate and layer diffraction peaks. The fringes are a measure of the high structural quality of the alloy layer and indicate that lattice planes and interfaces are uniform and flat.[49]

A simulated 004 HR-XRD $\omega$-$2\theta$ rocking curve, calculated based upon the fully dynamical formalism developed by Taupin[50] and Takagi,[51] is shown in Fig. 11(b) for comparison. The simulation was carried out assuming a perfectly planar and coherent film/substrate interface and interpolated elastic constants. B surface segregates with an enthalpy of $-0.53$ eV during Si(001):B film growth by GS-MBE from $B_2H_6/Si_2H_6$.[23] This results in the formation of a B-depleted region between the film/substrate interface and the film thickness at which a steady-state dopant incorporation rate is achieved.[52] The B-depletion zone slightly increases the scattered intensity in the $\omega$-$2\theta$ region between the layer and substrate peaks. We accounted for this in the XRD simulation using a linearly graded B-depleted layer which is, based upon SIMS depth profile results, 300 Å thick. The measured and simulated curves in Fig. 11 are in excellent agreement with respect to the positions and intensities of both the Bragg peaks and the finite-thickness interference fringes. From the fitted curve, we obtain, assuming Vegard's rule, a dopant concentration of $C_B = 2.8\times10^{20}$ cm$^{-3}$, which agrees well with the SIMS value of $2.5\times10^{20}$ cm$^{-3}$.

Figure 11(c) is a HR-XRD $\omega$-$2\theta$ scan from a 6500-Å-thick Si:B layer grown at $T_s = 600\,^\circ\mathrm{C}$ with $C_B = 4.2\times10^{21}$ cm$^{-3}$. The relative peak position and the full width at half maximum intensity $\Gamma_{\omega\text{-}2\theta}$ have increased from 235 and 25 arc s to 674 and 69 arc s, respectively, while the finite-thickness fringes have almost disappeared due to surface roughening.

Figure 12 shows typical high-resolution reciprocal lattice maps around the asymmetric 115 Bragg reflection from Si:B films with $C_B = 2.5\times10^{20}$ and $4.2\times10^{21}$ cm$^{-3}$. Diffracted intensity distributions are plotted as isointensity contours as a function of the reciprocal lattice wave vectors $k_\parallel$ parallel and $k_\perp$ perpendicular to the surface. For all samples, including the two ultrahighly doped films shown here, the substrate and film scattering distributions are nearly perfectly aligned in the $k_\parallel$ direction indicating negligible in-plane strain relaxation. From high precision measurements, the degree of strain relaxation is $<1\times10^{-4}$, near the instrument detection limit $2\times10^{-5}$, for all samples. Thus, the in-plane Si(001):B lattice constants $a_\parallel = 5.4310\pm0.0002$ Å are equal to that of bulk Si. The vertical separation between the film and substrate diffracted intensity distributions increases with $C_B$ indicating a tetragonal distortion. For the two layers corresponding to the data in Fig. 12, $a_\perp = 5.4180$ Å for the film with $C_B = 2.5\times10^{20}$ cm$^{-3}$ and 5.4055 Å with $C_B = 4\times10^{21}$ cm$^{-3}$.

Full width at half-maximum intensity values of the scattering intensity distributions along the $\omega$, $\omega$-$2\theta$, and in-plane $\parallel$ directions from the Si:B film in Fig. 12(a) ($C_B = 2.5\times10^{20}$ cm$^{-3}$) are $\Gamma_\omega = 12$ arc s, $\Gamma_{\omega\text{-}2\theta} = 38$ arc s, and $\Gamma_\parallel = 10$ arc s. The square root of the sum of these parameters

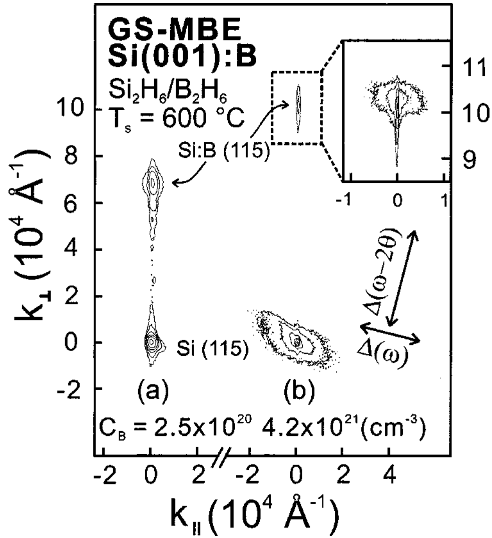


FIG. 12. High-resolution 115 reciprocal space maps from Si(001):B layers with B concentrations $C_B$ of (a) $2.5\times10^{20}$ cm$^{-3}$ and (b) $4.2\times10^{21}$ cm$^{-3}$. Successive isointensity contours correspond to 22000, 5000, 500, 80, 30, and 10 counts s$^{-1}$. The inset shows a detailed view of the layer peak in (b) with isointensity contours corresponding to 80, 45, 23, 7, and 2 counts s$^{-1}$.

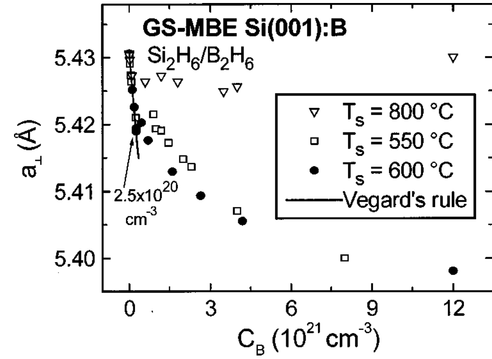


FIG. 13. The lattice constant $a_\perp$ along the growth direction as a function of B concentration $C_B$ for GS-MBE Si(001):B layers grown from $B_2H_6/Si_2H_6$ mixtures at $T_s=550$, 600, and 800 °C. The solid line shows Vegard's rule based upon a linear interpolation of diamond cubic Si and B lattice constants.

$\Gamma_t$ provides the best metric for comparing peak widths independently of peak shape.[53,54] For this layer, $\Gamma_t=41$ arc s, which is near the minimum theoretical value for this alloy, 21 arc s, calculated based upon the intrinsic peak width, 6 arc s while accounting for strain broadening due to lattice constant mismatch and finite thickness effects.[54] Peak-width values for the substrate diffracted intensity distribution in Fig. 12(a) are: $\Gamma_\omega=13$ arc s, $\Gamma_{\omega\text{-}2\theta}=22$ arc s, $\Gamma_\parallel=11$ arc s, with $\Gamma_t=28$ arc s. The similarity in film and substrate $\Gamma_\omega$ values indicates negligible film mosaicity.

Increasing $C_B$ to $4.2\times10^{21}$ cm$^{-3}$ [Fig. 12(b)] causes the peak separation to increase in the $k_\perp$ direction while the film remains coherent with the substrate. For this layer, $\Gamma_t=102.5$ arc s ($\Gamma_\omega=8.3$, $\Gamma_{\omega\text{-}2\theta}=102$, and $\Gamma_\parallel=6.1$ arc s) while $\Gamma_t$ for the substrate is 22.6 arc s ($\Gamma_\omega=10$, $\Gamma_{\omega\text{-}2\theta}=18.7$, and $\Gamma_\parallel=8$ arc s). $\Gamma_{\omega\text{-}2\theta}$ for the film peak is now an order of magnitude larger than the corresponding substrate value. However, $\Gamma_\omega$ and $\Gamma_\parallel$ remain near their minimum theoretical values, indicating lack of significant mosaicity. Furthermore, the integrated 115 Bragg intensity $I_{115}$ from the layer peak is weak and the diffuse scattering intensity at angles away from the Bragg peak is high. Thus, we interpret the large $\Gamma_t$ value from the layer as signifying the presence of large variations in the local microstrain[53] which, at these high-B concentrations, causes severe lattice-plane buckling distortions which reduce the 115 peak intensity.

Since all Si:B films are fully coherent with their substrate, $a_\perp$—plotted in Fig. 13 as a function of $C_B$ for layers grown at $T_s=550$, 600, and 800 °C—is a direct measure of the tetragonal strain associated with B-dopant incorporation. The curves show an initial linear ''Vegard's rule'' decrease in $a_\perp$ with increasing B concentration, but deviate significantly from linearity when $C_B$ exceeds a critical value $C_B^*$, which is $\simeq 2\times10^{20}$ cm$^{-3}$ at $T_s=550$ °C and $2.5\times10^{20}$ cm$^{-3}$ at 600 °C. The latter is consistent with transport measurements (Figs. 7 and 9) and $N_B$ vs $C_B$ results (Fig. 6) presented in Sec. III B showing that for 600 °C films with $C_B>2.5\times10^{20}$ cm$^{-3}$, an increasing fraction of the incorporated B resides in electrically-inactive sites. A detailed analysis, including an analytical model describing the $a_\perp(C_B)$ data in Fig. 13, is presented in Sec. VI A. Note, however, that the behavior of the $T_s=800$ °C films is clearly quite different, with $C_B^*$ reduced to $5\times10^{19}$ cm$^{-3}$.

Five ultrahighly doped GS-MBE Si(001):B layers grown at $T_s=600$ °C with fully electrically active B concentrations $C_B=2.5\times10^{20}$ cm$^{-3}$, well above the reported[6–8] equilibrium solid-solubility limits, were annealed in UHV at 600–1100 °C for times ranging up to 12 h. HR-XRD, reciprocal-lattice mapping, and Hall-effect analyses of the annealed layers showed that they remained fully coherent and all incorporated B still resides in substitutional sites. This suggests that the reaction path leading to B incorporation in electrically inactive sites proceeds through surface rather than bulk sites and that, once incorporated, the inactive species are frozen in the lattice at $T_s\leq600$ °C.

Plan-view 001 bright-field TEM micrographs of GS-MBE Si(001):B layers grown at $T_s=550$ and 600 °C with $C_B<1\times10^{20}$ cm$^{-3}$ are completely featureless. An example is presented in Fig. 14(a) for a film with $C_B=1\times10^{20}$ cm$^{-3}$. The selected-area electron diffraction pattern shown in the inset was obtained near the [001] zone axis and consists only of single-crystal reflections with symmetric intensities. $\bar{1}10$ XTEM images also show that the films are highly perfect [see, for example, Fig. 14(b)] with 111 lattice fringes, which are continuous across the film/substrate interface.

Similarly, TEM and XTEM analyses of films with even higher-B concentrations, up to the highest value grown ($C_B=1.2\times10^{22}$ cm$^{-3}$) were found, in agreement with HR-XRD results, to be free of misfit dislocations and B precipitates. The latter result indicates that B clusters, if present, must be smaller than $\simeq50$ Å. However, films with $C_B\geq2.5\times10^{20}$ cm$^{-3}$, in contrast to lower-doped layers, exhibit mottled dark contrast similar to that reported for ultrahighly B-doped Si ($C_B=3.5\times10^{20}$ cm$^{-3}$) grown by solid-source MBE.[55] Figure 15 is a typical XTEM dark-field image, acquired using a $\bar{g}=004$ diffraction vector, of a GS-MBE Si:B film grown at $T_s=600$ °C with $C_B=3\times10^{21}$ cm$^{-3}$. The image is representative of the entire sample, based upon over 100 fields of

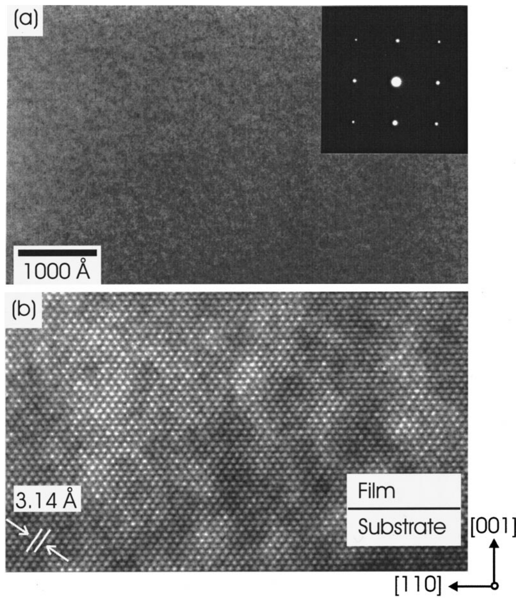


FIG. 14. (a) Plan-view 001 zone axis TEM micrograph of a GS-MBE Si(001):B layer with B concentration $C_B = 1 \times 10^{20}$ cm$^{-3}$ grown from $Si_2H_6/B_2H_6$ mixtures at $T_s = 600$ °C. The inset is a 001 selected-area electron diffraction pattern. (b) High-resolution XTEM micrograph from a GS-MBE Si(001):B layer grown at $T_s = 600$ °C with $C_B = 2.5 \times 10^{20}$ cm$^{-3}$.

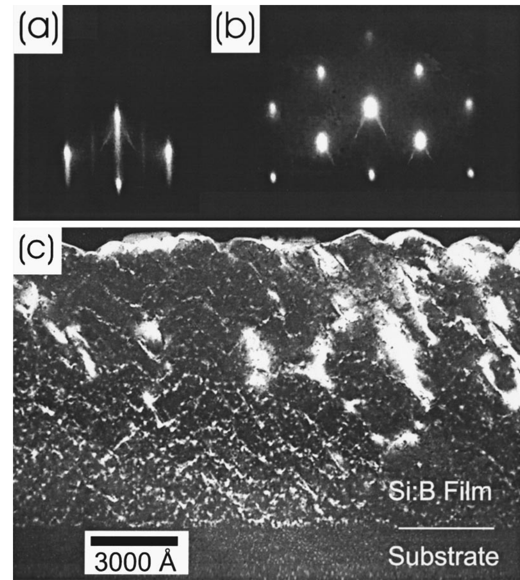


FIG. 16. RHEED patterns from GS-MBE Si(001):B layers grown at $T_s = 800$ °C with B concentrations $C_B$ of (a) $3 \times 10^{20}$ cm$^{-3}$ and (b) $3 \times 10^{21}$ cm$^{-3}$. (c) Dark-field 011 XTEM micrograph, acquired using the 004 reflection, of a B-doped GS-MBE Si(001) layer grown at $T_s = 800$ °C with $C_B = 3 \times 10^{21}$ cm$^{-3}$.

view. The film, even though it contains contrast variations throughout, appears everywhere darker than the substrate. The contrast arises from the enormous covalent radius misfit, −32%, between B and Si giving rise to large local atomic displacements of matrix atoms surrounding the B atoms in randomly distributed Si lattice sites. This, in turn, causes destructive interference among diffracted electron beams and results in reduced image brightness, particularly in dark-field imaging conditions.

While all layers grown at $T_s \leqslant 600$ °C exhibit smooth surfaces as in Fig. 15, we observe, by both RHEED and XTEM, extensive surface roughening in layers with $C_B > 5 \times 10^{19}$ cm$^{-3}$ grown at $T_s \geqslant 700$ °C. Pyramidal surface structures bounded by smooth 113 facets develop with increasing layer thickness. Figure 16(a) is a typical RHEED pattern obtained along a [110] direction of a 6000-Å-thick Si(001):B layer grown at 800 °C with $C_B = 3 \times 10^{20}$ cm$^{-3}$. Streaks, inclined at angles of 25.2° with respect to the surface normal and signifying the presence of 113 facets, are visible emanating from the tops and bottoms of both fundamental and half-order diffraction rods. At still higher-B concentrations, $C_B > 10^{21}$ cm$^{-3}$ [Fig. 16(b)], three-dimensional transmission diffraction patterns, indicative of an extremely rough surface, were observed at $T_s \geqslant 700$ °C.

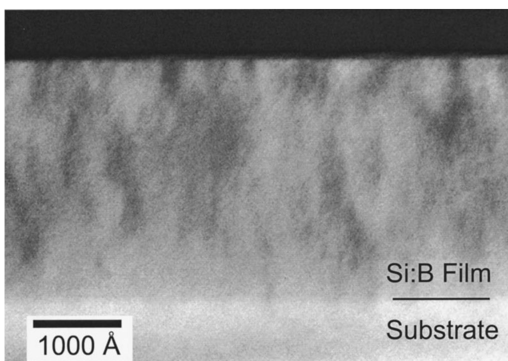


FIG. 15. Dark-field 011 XTEM micrograph, obtained using the 004 reflection, of a B-doped GS-MBE Si(001) layer grown at $T_s = 600$ °C with $C_B = 3 \times 10^{21}$ cm$^{-3}$.

An XTEM 110 dark-field image, acquired using a diffraction vector $\bar{g} = 004$, from a 9000-Å-thick layer grown at 800 °C with $C_B = 3 \times 10^{21}$ cm$^{-3}$ is shown in Fig. 16(c). The surface undulations have a wavelength of ≃1800 Å, with an average height of 400 Å. The slope of the facet surfaces is ≃25°, consistent with their being 113. XTEM micrographs show that layers exhibiting significant surface roughening also contain a large number density of dislocation loops and 111 stacking faults. These are clearly evident, for example, as bright contrast features in the dark-field XTEM micrograph in Fig. 16(c). Based upon $\bar{g} \cdot \bar{b}$ analyses, the loops are composed of 60° dislocations with ⟨110⟩ Burgers's vectors $\bar{b}$. The loops are not directly responsible for appreciable strain relaxation since they do not form misfit dislocation segments at the film/buffer-layer interface.[56] Nevertheless, Fig. 13 reveals that the degree of strain in ultrahighly doped Si(001):B layers grown with $C_B > 5 \times 10^{19}$ cm$^{-3}$ at $T_s = 800$ °C is relatively low compared to similarly doped 600 °C films.

The dislocation loops are similar to those observed in annealed B-implanted Si wafers[13] where the loops form when implantation-induced-interstitials condense during subsequent annealing. Transient enhanced diffusion[13,18] (TED) of B occurs during annealing in the presence of Si self-interstitial concentrations estimated to be as high as $10^{19}$ cm$^{-3}$.[57] TED is associated with B cluster formation in bulk Si through the formation of fast-diffusing substitutional-

B/interstitial-Si complexes[13] which can interact with substitutional B atoms to form split-substitutional B pairs and possibly larger clusters[13,18] (in all cases smaller than the TEM resolution limit, $\simeq$50 Å). In the present experiments, we show in Sec. IV A that the B pairs impart a small compressive in-plane strain on the Si(001) lattice. Thus, nanoscale B clustering via TED combined with B decoration of dislocation loops and stacking faults during growth at high temperatures results in reduced in-plane tensile strain and electrical activity in ultrahighly doped films.

## IV. DISCUSSION

We have shown that during GS-MBE of Si(001):B from $Si_2H_6/B_2H_6$ mixtures, B is incorporated into electrically active lattice sites via a thermally activated reaction path for concentrations $C_B$ up to $C_B^*$. The incorporated B strongly segregates to the second layer where the steady-state coverage $\theta_B$ increases with $C_B$ to reach saturation, $\theta_{B,sat}=0.5$ ML, when $C_B=C_B^*$. At $T_s=600\,^\circ$C, $C_B^*$ is $2.5\times10^{20}$ cm$^{-3}$ and $\theta_{B,sat}$ occurs with an incident flux ratio $J_{B_2H_6}/J_{Si_2H_6}$ of 0.25. With further increases in the flux ratio, segregated B in excess of $\theta_{B,sat}$ goes to the first layer where it affects the reaction path of subsequently adsorbed $B_2H_6$ and results, as discussed below, in the incorporation of nonelectrically active B.

$C_B$ increases linearly with $J_{B_2H_6}/J_{Si_2H_6}$ up to a ratio of 0.25 at $T_s=600\,^\circ$C, and more rapidly at higher flux ratios. Over the linear range, $C_B$ is equal to $N_B$, the electrically active B concentration, while at higher total B concentrations, $N_B$ becomes progressively smaller than $C_B$. HR-XRD measurements show that $a_\perp$ decreases linearly with $C_B$ for values $\leqslant C_B^*$ while at higher B concentrations, there is a discontinuous change in $a_\perp(C_B)$ and the curve becomes nonlinear. The sum of these results indicates that for film growth conditions giving rise to total doping concentrations above $C_B$, B incorporation occurs through at least two parallel reaction paths.

For most common $p$- and $n$-type dopants, including Al, Ga, P, and Sb, the electrically active dopant fraction progressively decreases as the total doping concentration is increased above the kinetic solubility limit.[58] This is due to the formation of precipitates, which, once nucleated, act as sinks for dopant atoms and thus decrease the doping concentration in substitutional Si sites.[59] In the present case, however, the electrically active dopant concentration continues to increase even though the active fraction decreases dramatically. Moreover, extensive TEM analyses, in both low- and high-resolution modes, of samples with $C_B>C_B^*$ reveal no evidence of B precipitates, implying that, if present, they must be in the form of small ($\lesssim$50 Å, the TEM detection limit for low-$Z$ elements) dispersed nanoclusters.

Temperature-dependent Hall measurements carried out on layers grown with $C_B\leqslant C_B^*$ at $T_s=600\,^\circ$C demonstrate that hole mobilities are equal to, or better than, the best bulk Si:B values up to the highest doping concentrations reported and, for layers with higher concentrations, equal to theoretical values. Moreover, the room-temperature hole mobility remains essentially constant even as $C_B$ is increased almost an order of magnitude above $C_B^*$ to $1.6\times10^{21}$ cm$^{-3}$ for which the inactive dopant concentration ($C_B-N_B$) is $4.8\times10^{20}$ cm$^{-3}$ ($N_B/C_B=0.3$), demonstrating that electrically inactive B has a small charge scattering cross section. As $C_B$ is increased further, however, the film resistivity increases and the hole mobility decreases rapidly indicating the onset of an additional carrier scattering mechanism which, based upon HR-XRD and TEM contrast analyses, is strain-induced disorder.

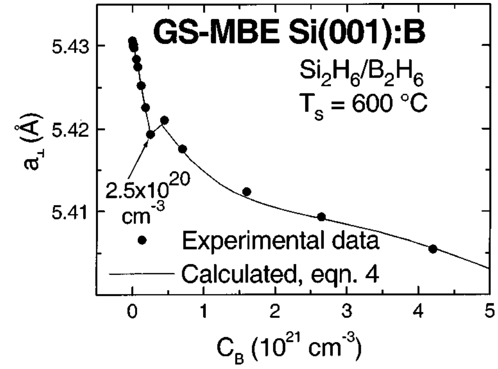


FIG. 17. The lattice constant $a_\perp$ along the growth direction as a function of B concentration $C_B$ in GS-MBE Si(001):B layers grown from $Si_2H_6/B_2H_6$ mixtures at $T_s=600\,^\circ$C. The solid line was calculated using Eq. (4).

### A. B-induced strain and microstructural changes

Tensile strain in Si associated with B doping at concentrations above $\simeq5\times10^{18}$ cm$^{-3}$ is quantitatively measurable by HR-XRD. The rate of change in the macroscopic strain state provides useful insights regarding the lattice site, as well as the ensemble, into which B is incorporated. In Sec. III E, we showed using high-resolution reciprocal lattice maps obtained from asymmetric reflections that all films remain fully commensurate, even up to the highest B concentrations investigated, 24 at. %. The in-plane Si:B layer lattice constants are identical to those of the Si substrate within one part in $10^4$. However, as shown in Fig. 17, the out-of-plane lattice parameter $a_\perp$ decreases linearly with $C_B$, consistent with Vegard's rule, demonstrating (together with the combined SIMS and Hall-effect results in Fig. 6) that all B is incorporated into electrically active substitutional sites for concentrations up to $C_B^*$. The data in this range are very well fit with the expression

$$a_\perp=a_{Si}+\beta N_B, \tag{2}$$

for which $a_{Si}$ is the bulk Si lattice parameter (5.4310 Å) and $N_B$ is the active B concentration. $\beta$, the strain rate coefficient, is given by

$$\beta=\left[\left(\frac{1+\nu_{Si}}{1-\nu_{Si}}\right)\left(\frac{a_B-a_{Si}}{n_{Si}}\right)\right]. \tag{3}$$

$\nu_{Si}$ and $n_{Si}$ in Eq. 3 are the Poisson ratio (0.278) and atomic density ($5\times10^{22}$ cm$^{-3}$) of Si while $a_B$ is the lattice constant of diamond structure B (4.10 Å) calculated using the B tetrahedral covalent radius, 0.88 Å.[60] Substituting these terms into Eq. (3) yields a value for $\beta$ of $-4.02\times10^{-23}$ Å cm$^3$ in very good agreement with the best

fit value in Fig. 17 of $-4.5\times10^{-23}$ Å cm$^3$. The experimentally determined value of $\beta$ was used to calculate the Si-B bond length $r_{\text{Si-B}}=2.04\pm0.02$ Å following the procedure outlined in Appendix A. The result is within the range of that reported by Weir *et al.*,[61] $r_{\text{Si-B}}=2.0$–$2.1$ Å based upon an analysis of glancing-angle XRD patterns obtained from an ordered Si(001):B monolayer containing 0.5 ML of B.

As $C_B$ is increased above $C_B^*$, $a_\perp$ continues to decrease, but at a slower rate, and $a_\perp(C_B)$ becomes nonlinear with B incorporated into *both* electrically active and inactive sites. A comparison of the $a_\perp$ vs $C_B$ relationships for $C_B$ less than and greater than $C_B^*=2.5\times10^{20}$ cm$^{-3}$ at $T_s=600\,°\mathrm{C}$ shows that while the incorporation of electrically active B results in purely tensile in-plane strain, electrically inactive B in the configuration gives rise to compression.

Detailed plan-view and cross-sectional TEM analyses, including high-resolution, were carried out on representative samples spanning the entire B concentration and growth-temperature ranges investigated. Consistent with the HR-XRD results, there was no evidence of precipitates or misfit dislocations in any sample. For layers with $C_B \lesssim 2\times10^{20}$ cm$^{-3}$, the Si:B film/buffer-layer interface is essentially indiscernible, even under dark-field imaging conditions.

The full set of $a_\perp(C_B)$ data, including the kink in the curve signifying the point at which inactive B first begins to be incorporated, is well described, as shown in Fig. 17, by the addition of another term to Eq. (3) to yield

$$a_\perp = a_{\mathrm{Si}} + \beta N_B + \alpha(C_B - N_B). \tag{4}$$

$\alpha$, the inactive-B strain coefficient, is $4.8\times10^{-24}$ Å cm$^3$. The fact that the entire curve, linear plus nonlinear portions, can be fit with a single value of $\alpha$ suggests that all inactive B is incorporated into a single type of configuration, whose size remains constant irrespective of $C_B$.

The value of $\alpha$ obtained from Eq. (4) and Fig. 17 was used to test potential B cluster bonding configurations. TEM and electronic transport data rule out the presence of large B clusters. Of the small cluster sizes that theory indicates may be stable—clusters with 2, 3, 6, and 12 atoms[15,16,18,62,63]—only B pairs are consistent with our measured strain behavior. This is in agreement with recent *ab initio* local-density approximation calculations,[18,62] as well as tight-binding computations employing the Stillinger-Weber potential,[63] which predict that the most stable B clusters in Si are B pairs. The lowest-energy B-pair configuration is the split substitutional in which the B-B bond is oriented along ⟨100⟩ with bond lengths $r_{\text{Si-B}_{\text{pair}}}=2.01$ and $r_{\text{B-B}}=1.60$ Å.[18,62]

In a bulk crystal, such as was assumed in the above calculations, there is no reason to expect an anisotropy in the ⟨100⟩ orientations of B-B dimer bonds. A strained layer, however, can induce a preferential B-B bond orientation, which, in the present case with the films in tension, would correspond to the [001] growth direction. Alternatively, the B-B orientation may be controlled by the reaction path of the incorporating B pair such that its orientation is frozen before film strain can play a role.

We have computed (see Appendix A), based upon the strain coefficient $\alpha$ determined from Eq. (4), the bond length $r_{\text{Si-B}_{\text{pair}}}$ between nearest-neighbor Si and paired B atoms for three cases: (1) all B pairs aligned along the [001] growth direction, (2) all B pairs aligned in-plane and distributed equally along [100] and [010] directions, and (3) B pairs distributed randomly in the three orthogonal directions. The results yield $r_{\text{Si-B}_{\text{pair}}}=1.70$, 2.18, and $2.01\pm0.04$ Å, respectively. $r_{\text{Si-B}_{\text{pair}}}$ for case (1) can be dismissed immediately since it is 15% less than $r_{\text{Si-B}}$ and therefore unphysical. $r_{\text{Si-B}_{\text{pair}}}$ for case (3), however, is in agreement with total energy calculations for randomly aligned ⟨100⟩ B pairs[62] suggesting that non-electrically active-B is incorporated into GS-MBE Si(001) as B pairs in substitutional lattice sites in which the B-B bonds are distributed equally along the three cube axes. This is consistent with the continued increase, although at a slower rate, in $N_B$ with increasing $C_B > C_B^*$ through parallel B and B-pair reaction channels. The B pairs would have an $sp^2$-bonded trigonally-coordinated symmetry in agreement with our near-edge x-ray absorption fine structure measurements.[64] Moreover, B is trivalent and should therefore be electrically inactive, as we observe experimentally, due to being bond saturated in this configuration.

Dark-field $\bar{g}=004$ XTEM micrographs obtained from layers with $C_B \gtrsim 2\times10^{20}$ cm$^{-3}$, while free of precipitates and misfit dislocations, exhibit a mottled dark contrast with respect to the substrate (Fig. 15). Correspondingly, increasing $C_B$ in this concentration range results in HR-XRD Bragg peaks from the film becoming broader and less intense as more diffuse scattering is observed. Reciprocal lattice maps show that peak broadening is particularly pronounced in the $\omega$-$2\theta$ direction indicating a wide distribution of interplanar spacings. We interpret this as being due to lattice plane buckling in the presence of a high concentration of localized B-induced strain fields.

### B. Boron incorporation kinetics

We have previously published a detailed predictive model, with no fitting parameters, for the deposition rate $R$ of GS-MBE Si(001) as a function of incident $Si_2H_6$ flux $J_{Si_2H_6}$ and film growth temperature $T_s$.[65] The model contains terms accounting for a stepwise reaction path including dissociative chemisorption, a series of surface decomposition reactions, and first-order $H_2$ desorption from Si monohydride. The $Si_2H_6$ reactive sticking probability $S_{Si_2H_6}$ exhibits a small negative activation energy, $E_{\mathrm{Si}} \approx -0.16$ eV,[66] indicating that chemisorption is precursor mediated.

The Si(001) growth kinetics model was later extended to predict B concentrations incorporated from $Si_2H_6/B_2H_6$ mixtures during Si(001):B deposition with $C_B\times10^{19}$ cm$^{-3}$.[19] $B_2H_6$ chemisorption, in analogy with $Si_2H_6$ results, is taken to be second order in this concentration range and the reactive sticking probability is thermally activated (unlike the case for $Si_2H_6$) with a small positive activation energy, $E_B=0.18$ eV. $S_{B_2H_6}$ and $S_{Si_2H_6}$ were found to be independent leading to the following simple expression for $C_B$,

$$C_{B,\mathrm{calc}} = \frac{S_{B_2H_6} J_{B_2H_6}}{S_{Si_2H_6} J_{Si_2H_6}} n_{\mathrm{Si}}, \tag{5}$$

in which $n_{\mathrm{Si}}$ is the atomic density of Si, $5\times10^{22}$ cm$^{-3}$. Figure 2 shows that the $\ln(C_B)$ vs $J_{B_2H_6}/J_{Si_2H_6}$ results obtained

in the present experiments are well described by Eq. (5) for B concentrations up to $C_B^*$. Values for $S_{Si_2H_6}(T_s)$ and $S_{B_2H_6}(T_s)$ were taken from Refs. 66 and 19, respectively. Note that the overall temperature-dependence for B incorporation in Eq. (5) enters simply through the difference between the activation energies for B and Si chemisorption, where $E_B^{inc} = E_B - E_{Si} = 0.34$ eV.

The $C_B$ vs $1/T_s$ data in Fig. 3, obtained with $J_{B_2H_6}/J_{Si_2H_6}$ ratios ranging from $9.3 \times 10^{-5}$ to 0.25, are in excellent agreement with Eq. (5). That is, the slopes of these curves remain constant yielding $E_B^{inc} = 0.34 \pm 0.01$ eV. The reaction path for B incorporation into electrically active sites in this concentration range proceeds through a B-induced ordered $c4 \times 4$ reconstruction in the second layer,[23] with a maximum coverage of 0.5 ML, which serves as the reservoir for B incorporation into ''bulk'' substitutional sites.

Figure 3 also shows that $E_B^{inc}$ is no longer constant at $J_{B_2H_6}/J_{Si_2H_6}$ values $\geqslant 0.3$. In this range, $E_B^{inc}$ decreases continuously, indicating the onset of a parallel incorporation path that is precursor mediated, and actually becomes negative for $J_{B_2H_6}/J_{Si_2H_6} \gtrsim 2$. At the highest flux ratio used in these experiments, $J_{B_2H_6}/J_{Si_2H_6} = 3.0$, $E_B^{inc}$ reaches a value of $-0.06$ eV. $J_{B_2H_6}/J_{Si_2H_6} \geqslant 0.3$ corresponds to deposition conditions, over the growth-temperature range 550–800 °C, for which B segregation results in second-layer coverage which exceed $\theta_{B,sat}$ with the excess B occupying sites at the outer surface.[22,23]

The inset in Fig. 6 shows that while the electrically active B fraction $N_B/C_B$ decreases rapidly with $C_B > C_B^*$, the total (active plus inactive) B incorporation rate increases as a function of $J_{B_2H_6}/J_{Si_2H_6}$ (see inset in Fig. 2). The two results are correlated, and together with post-annealing data showing that $N_B/C_B$ remains constant, indicate that electrically inactive B is incorporated directly from the growth surface rather than forming in the bulk. Furthermore, the fact that we observe $N_B/C_B$ to increase with increasing $T_s$ is circumstantial evidence that inactive B is chemisorbed directly as B pairs, i.e., $B_2H_6$ absorption kinetics become precursor mediated rather than thermally activated in the presence of surface B. (If $B_2H_6$ adsorption remained second order and B pairs formed via surface diffusion and recombination, then we would expect $N_B/C_B$ to decrease with $T_s$ due simply to a higher B-B encounter probability.)

The total B incorporation probability can be expressed as the product of the individual incorporation probabilities for electrically active B, $S_{B_2H_6}^{B}$, and inactive B, $S_{B_2H_6}^{B\text{-}B}$, where

$$S_{B_2H_6} = (S_{B_2H_6}^{B})^{f_a} (S_{B_2H_6}^{B\text{-}B})^{(1-f_a)} \tag{6}$$

and $f_a$ and $(1-f_a)$ are the measured fractions of electrically active and inactive B. This leads to an expression (see Appendix B) for the overall activation energy [i.e., the slope of the ln($C_B$) vs $J_{B_2H_6}/J_{Si_2H_6}$ curves in Fig. 3] given by

$$E_B^{inc} = \{f_a E_B + (1-f_a) E_{B\text{-}B}\} - E_{Si} + K, \tag{7}$$

where $E_{B\text{-}B}$ is the rate-limiting activation energy for B incorporation as electrically-inactive B pairs on substitutional Si lattice sites and $K$ is a temperature-independent constant. All data in Figs. 2 and 3, covering the entire range of $J_{B_2H_6}/J_{Si_2H_6}$ and $T_s$ values investigated in these experiments, including that corresponding to $C_B > C_B^*$, are very well described by the combination of Eqs. (5)–(7) with $E_{B\text{-}B} = -0.23 \pm 0.04$. Calculated results are represented in Fig. 3 by solid lines.

### C. High-temperature growth ($T_s \geqslant 700$ °C)

The reaction path for B incorporation into Si at ultrahigh doping concentrations becomes more complex at growth temperatures $T_s \geqslant 700$ °C. This is most easily seen by comparing results obtained at $T_s = 600$ and 800 °C in Fig. 13. At the lower growth temperatures, all B atoms are incorporated into substitutional electrically active sites at concentrations $C_B$ up to $C_B^*$ ($2.5 \times 10^{20}$ cm$^{-3}$ at $T_s = 600$ °C) corresponding to the point at which $\theta_B$ in the second layer reaches $\theta_{B,sat} = 0.5$ ML. As $C_B$ is increased above $C_B^*$ with $T_s < 700$ °C, excess B segregates to the outer surface[23] allowing direct incorporation of B in the form of electrically inactive clusters (see discussion, Sec. IV B). This occurs in addition to (but not at the expense of) the continued incorporation of substitutional electrically active B from the second layer. The overall B incorporation changes at $T_s \geqslant 700$ °C, however, as B is found to reside in electrically-inactive sites when $\theta_B < \theta_{B,sat}$; that is, in the absence of B at the outer surface.

For all growth temperatures used in these experiments, B segregation is in the equilibrium regime[23] and, hence, the B segregation ratio decreases with increasing $T_s$. Thus, the B concentration $C_B^*$ at which $\theta_B$ reaches saturation increases with $T_s$.[52] In addition, Fig. 2 shows that the degree of deviation from a linear variation in $C_B$ as a function of $J_{B_2H_6}/J_{Si_2H_6}$ decreases with increasing $T_s$. Both of these effects would favor higher electrically active B concentration with a correspondingly higher strain at $T_s = 800$ °C than at 600 °C. However, as shown by the results in Fig. 13, we observe the opposite. The B concentration at which both $a_\perp(C_B)$ and $N_B(C_B)$ become nonlinear and at which B begins to be incorporated into non-electrically-active sites is reduced from $2.5 \times 10^{20}$ cm$^{-3}$ at $T_s = 600$ °C to $5 \times 10^{19}$ cm$^{-3}$ at 800 °C.

A strong clue toward explaining the B incorporation behavior at high-growth temperatures derives from XTEM micrographs [Fig. 16(c)] showing that layers exhibiting significant surface roughening also contain a large number density of dislocation loops and 111 stacking faults. It is well documented that the presence of dislocation loops of the type observed in Fig. 16(c) indicate high-Si self-interstitial concentrations.[13,60] The interstitials deactivate B acceptors in a TED-like clustering mechanism, as well as by inducing extended defects that are subsequently decorated by B atoms. The injection mechanism for Si self interstitials at concentrations in excess of equilibrium values appears to be related to surface roughening. It is clear that this is not a purely thermal effect since post-annealing (up to 1100 °C for 12 h) of 100% electrically active B-doped Si(001) layers grown at 600 °C with $C_B = 2 \times 10^{20}$ cm$^{-3}$ and smooth surfaces did not result in any measurable loss in electrical activity.

The above phenomena, including the formation of dislocation loops, are not observed during growth of ultrahighly doped Si(001):B at $T_s \leqslant 600$ °C due to both thermal quench-

ing and H-induced reduction of adatom surface mobilities.[67] Low-growth temperatures, with their associated high steady-state H coverages, do not provide the thermal activation necessary for the massive uphill diffusional transport of atoms required for roughening.[56] At these temperatures, complete electrical activity is maintained for B concentrations up to $C_B^*$.

### D. Transport properties

The quantitative agreement between the total incorporated B concentration $C_B$, obtained independently from SIMS and HR-XRD measurements, and active B concentrations $N_B$ determined from Hall-effect results at $C_B=N_B \leqslant 2.5\times10^{20}$ cm$^{-3}$ for GS-MBE Si(001):B films grown at $T_s=600\,°$C indicates that all B atoms in these layers occupy substitutional electrically active sites in the Si lattice. This is further substantiated by the good agreement in Figs. 7 and 9 between our measured $\rho(C_B)$ and $\mu(C_B)$ results and theoretical predictions. Room-temperature hole mobilities were found to be equal to maximum theoretical values up to the limit of 100% B activation, $C_B^*=2.5\times10^{20}$ cm$^{-3}$, and $\mu_{300\,K}$ remained essentially constant for B concentrations even up to almost an order of magnitude higher. This is consistent with inactive B being incorporated as pairs on substitutional Si sites. Such a configuration is expected to lead to relatively small carrier scattering cross sections since the defect is neutral and resides on a substitutional site. $\mu_{300\,K}$ ranges from 168 to 47 to 41 to 8 cm$^2$ V$^{-1}$ s$^{-1}$ at $C_B=1.7\times10^{17}$, $2.5\times10^{20}$, $1.6\times10^{21}$, and $1.2\times10^{22}$ cm$^{-3}$, respectively.

While $\mu_{300\,K}$ remains approximately constant over the B concentration range between $\simeq2.5\times10^{20}$ and $1.6\times10^{21}$ cm$^{-3}$ ($N_B/C_B=1$ to 0.3), it decreases abruptly at higher B concentrations. The decrease is due to additional charge scattering resulting from the breakdown in long-range order due to the high density of randomly distributed local strain fields emanating from lattice dilatations caused by B and B pairs residing on substitutional Si sites. The distribution of Si bond lengths and angles becomes progressively wider with increasing $C_B$ at these very high B concentrations.

Temperature-dependent hole mobilities were shown to vary smoothly from being characteristic of itinerant hole transport when $C_B$ is less than $\lesssim3\times10^{18}$ cm$^{-3}$ to hopping conductivity for $C_B\simeq3\times10^{18}-10^{19}$ cm$^{-3}$ to metallic at higher concentrations. In the itinerant hole transport regime, $\mu$ is primarily limited by lattice scattering near room temperature and ionized-impurity scattering at low temperatures. As $C_B$ is increased, the transition from phonon-dominated to ionized-impurity dominated scattering shifts to progressively higher temperatures. With $C_B$ above $3\times10^{18}$ cm$^{-3}$, band-tailing significantly reduces carrier freeze out thereby increasing the number density of filled acceptor states sufficiently to allow hopping conduction over the entire measured temperature range. This puts a lower limit on hole mobility. Further increases in $C_B>10^{19}$ cm$^{-3}$ shifts the conductivity into the metallic regime.

## V. CONCLUSIONS

Si(001) layers doped with B concentrations $C_B$ between $1\times10^{17}$ and $1.2\times10^{22}$ cm$^{-3}$ were grown on Si(001)2×1 at temperatures $T_s=500-850\,°$C by GS-MBE from $Si_2H_6$ and $B_2H_6$. $C_B$ increases linearly with the incident precursor flux ratio $J_{B_2H_6}/J_{Si_2H_6}$ and, for $T_s<700\,°$C, B is incorporated into substitutional electrically-active sites at concentrations up to $C_B^*$. For $T_s=600\,°$C, $C_B^*$ is $2.5\times10^{20}$ cm$^{-3}$. At higher-B concentrations, $C_B$ increases faster than $J_{B_2H_6}/J_{Si_2H_6}$ and there is a large and discontinuous decrease in the electrically active fraction of incorporated B. However, the total activated B concentration continues to increase and reaches a value of $N_B=1.3\times10^{21}$ cm$^{-3}$ with $C_B=1.2\times10^{22}$ cm$^{-3}$. Resistivities are in good agreement with theoretical values to $C_B^*$ for which $\rho_{300\,K}=300\,\mu\Omega$ cm. Conductivity mobilities are equal to theoretical maximum values to $C_B=1.6\times10^{21}$ cm$^{-3}$. HR-XRD and reciprocal space mapping measurements show that all films are fully strained. No B precipitates, or misfit dislocations, were detected by HR-XRD and TEM analyses, even in films with $C_B=1.2\times10^{22}$ cm$^{-3}$(24 at % B). The lattice constant in the film growth direction $a_\perp$ decreases linearly with increasing $C_B$ up to the limit of full electrical activation and continues to decrease, but nonlinearly, with $C_B>C_B^*$.

HR-XRD, SIMS, Hall-effect, and TEM data were used in concert to determine the nature and lattice site of electrically inactive B. We find from TEM/XTEM analyses that B clusters must be smaller than $\simeq$50 Å, from HR-XRD that the macroscopic strain contribution per inactive B atom is constant, and from Hall measurements that the active B concentration continues to increase even when $C_B>C_B^*$. These results indicate that B is present in small highly dispersed nanoclusters of constant size. Based upon a detailed analysis of the out-of-plane Si(001):B lattice constants as a function of active and inactive B concentrations, we show that inactive B is incorporated as trigonally coordinated B pairs on single Si sites and oriented with the B-B bond axis randomly aligned along $\langle001\rangle$ directions.

The fraction of inactive B decreases with increasing temperature indicating that the B pairing reaction is not diffusion controlled. Furthermore, the B concentration as a function of $J_{B_2H_6}/J_{Si_2H_6}$ becomes superlinear when $\theta_B>\theta_{B,sat}$ and the net increase in $C_B$ is essentially equal to the concentration of inactive B. These factors support direct B pair incorporation at the growth surface. During high-temperature growth ($T_s \geqslant 700\,°$C), the situation is more complex. In addition to direct B incorporation at the surface, B clustering in the bulk is mediated by large concentrations of interstitial point defects resulting in B deactivation during growth when $C_B$ exceeds $5\times10^{19}$ cm$^{-3}$.

B strongly surface segregates to the second layer with a saturation coverage $\theta_{B,sat}$ of 0.5 ML (corresponding to $C_B=C_B^*$ for $T_s<700\,°$C). At higher $C_B$, $\theta_B>\theta_{B,sat}$ and B accumulates in the upper layer, as shown by thermally programmed desorption measurements. The presence of upper layer B modifies the interaction of $B_2H_6$ with the Si surface, and opens a parallel reaction channel whereby B incorporates as pairs which are electrically inactive but have a low carrier scattering cross section. At $C_B>2\times10^{21}$ cm$^{-3}$ carrier mobilities begin to degrade substantially. This is correlated with lattice plane buckling in response to local B-induced strain measured by x-ray diffraction as well as by TEM electron diffraction contrast measurements.

## ACKNOWLEDGMENTS

The authors gratefully acknowledge the financial support of the Semiconductor Research Corporation and the U.S. Department of Energy, Division of Materials Sciences (Award No. DEFG02-ER9645439). We also appreciate the use of the Center for Microanalysis of Materials, partially supported by DOE, at the Frederick Seitz Materials Research Laboratory (UI). P.D. was partially supported by NSERO (Canada).

## APPENDIX A

The Si-B bond length in Si:B was calculated based upon the $\beta$ value obtained from the $a_\perp(C_B)$ data in Fig. 17 and Eq. (4) using the following procedure. The lattice parameter for a hypothetical zinc-blende-structure $Si_{0.5}B_{0.5}$ alloy, in which every bond is between neighboring Si and B atoms, was obtained by linear extrapolation of the $a_\perp$ vs $C_B$ curve in Fig. 17 to $C_B = N_B = N_{Si}/2 = 2.5 \times 10^{22}$ cm$^{-3}$. The tetragonally strained unit cell was converted to a cubic cell using the Poisson ratio for Si, $v_{Si} = 0.278$, and assuming linear elasticity. The cubic lattice parameter was then used to calculate the Si-B bond length given the 109.5° tetrahedral bond angle. The result yields $r_{\text{Si-B}} = 2.04$ Å.

The bond length $r_{\text{Si-B}_{\text{pair}}}$ between nearest-neighbor Si and B-pair B atoms was calculated using an analogous procedure. We determined $a_\perp$ for a hypothetical ordered $Si_{0.33}B_{0.66}$ alloy composed of Si and B-pairs as basis sets on substitutional zincblende sites. This was done by extrapolating $a_\perp(C_B)$ to the value corresponding to $C_B = 2N_{Si}/3$ with $N_B = 0$. The tetragonal cell was converted to cubic as described above. $r_{\text{Si-B}_{\text{pair}}}$ values were then calculated for different B-pair bond-axis orientation distributions based upon the cubic cell volume with a B-B bond length of 1.60 Å (Refs. 18 and 67) and trigonal Si-B-Si bond angles of 120°. Three cases were considered: (1) all B pairs aligned with their bond axes along the [001] growth direction, (2) B pairs aligned randomly along in-plane [100] and [010] directions, and (3) B pairs distributed equally in all three orthogonal ⟨100⟩ directions. In the latter case, a supercell of three unit cells was used. The results for $r_{\text{Si-B}_{\text{pair}}}$ are (1) 1.70, (2) 2.18, and (3) 2.01 Å.

## APPENDIX B

We have previously shown that B segregates strongly to the second layer during Si(001):B film growth.[21,22] The process is well described by Gibbsian equilibrium segregation theory with a saturation B second-layer coverage $\theta_{B,sat}$ of 0.5 ML and a segregation enthalpy of $-0.53$ eV.[23] The bulk B concentration $C_B$ corresponding to $\theta_{B,sat}$ ranges from $2\times10^{20}$ cm$^{-3}$ at $T_s = 550\,^\circ$C to $7\times10^{20}$ cm$^{-3}$ at $T_s = 800\,^\circ$C When $C_B$ exceeds these concentrations (i.e., when $\theta_B > \theta_{B,sat}$), B begins to accumulate at the outer surface.

In the absence of B at the outer Si(001) surface, $B_2H_6$ dissociatively chemisorbs in a second-order thermally activated process to yield B atoms which, mediated by second-layer segregation, move to substitutional electrically active sites. However, the presence of B at the outer layer strongly affects the $B_2H_6$ adsorption process and introduces an additional B incorporation path which is precursor mediated and results in the incorporation of electrically inactive B pairs in substitutional sites. The overall B reactive sticking probability $S_{B_2H_6}$ can be expressed as

$$S_{B_2H_6} = (S^{B}_{B_2H_6})^{f_a} (S^{\text{B-B}}_{B_2H_6})^{(1-f_a)}, \tag{B1}$$

where $S^{B}_{B_2H_6}$ is the reactive sticking probability leading to single B atom incorporation, $S^{\text{B-B}}_{B_2H_6}$ is the reactive sticking probability leading to B-pair incorporation, $f_a$ is the electrically active fraction of incorporated B, and $(1-f_a)$ is the fraction of B present in the form of B pairs. When $\theta_B \leqslant \theta_{B,sat}$, $f_a = 1$ and $S_{B_2H_6} = S^{B}_{B_2H_6}$. As $\theta_B$ exceeds 0.5 ML, $f_a$ decreases exponentially with increasing $C_B$ (see inset in Fig. 6). $f_a$ also depends on the film growth temperature through the B segregation rate. Thus, since we are in the equilibrium segregation regime,[52] $\theta_B$ decreases with increasing $T_s$ for a given value of $C_B$ resulting in an increase in $f_a(T_s)$.

The total fraction $x_B$ of B incorporated into the Si lattice is given by the ratio of the B to Si reactive sticking probabilities,

$$x_B = \frac{S_{B_2H_6}}{S_{Si_2H_6}} = \frac{(S^{B}_{B_2H_6})^{f_a} (S^{\text{B-B}}_{B_2H_6})^{(1-f_a)}}{(S_{Si_2H_6})}. \tag{B2}$$

Extracting the rate constants from the activated reactive sticking probabilities yields

$$e^{(-E^{\text{inc}}_B/kT)} \propto \frac{(e^{(-E_B/kT)})^{f_a} (e^{(-E_{\text{B-B}}/kT)})^{(1-f_a)}}{e^{(-E_{Si}/kT)}}, \tag{B3}$$

where $E_B$, $E_{\text{B-B}}$, and $E_{Si}$ are the activation energies for incorporation of B, B pairs, and Si while $E^{\text{inc}}_B = (E_B - E_{Si})$. Taking the natural logarithm of both sides and rearranging terms, we obtain

$$\begin{aligned} E^{\text{inc}}_B &= f_a(E_B - E_{Si}) + (1-f_a)(E_{\text{B-B}} - E_{Si}) + K \\ &= \{f_a E_B + (1-f_a) E_{\text{B-B}}\} - E_{Si} + K, \end{aligned} \tag{B4}$$

in which $K$ is constant with respect to temperature.

[1] T. Uchino, T. Shiba, T. Kikuchi, Y. Tamaki, A. Watanabe, and Y. Kiyota, IEEE Trans. Electron Devices **42**, 406 (1995).

[2] Z. Matutinovickrstelj, V. Venkataraman, E. J. Prinz, J. C. Sturm, and C. W. Magee, IEEE Trans. Electron Devices **43**, 457 (1996).

[3] Y. Kinoshita, K. Imai, H. Yoshida, H. Suzuki, T. Tatsumi, and T. Yamazaki, in *International Electronic Devices Meeting*, 1994, Technical Digest (IEEE, N.Y., 1994), p. 441.

[4] Y. Kiyota, T. Nakamura, S. Suzuki, and T. Inada, IEICE Trans. Electron. **E79C**, 554 (1996).

[5] R. R. A. Syms, B. M. Hardcastle, and R. A. Lawes, Sens. Actuators A **63**, 61 (1997).

[6] S. M. Sze, *Physics of Semiconductor Devices*, 2nd ed. (Wiley,

New York, 1981).
[7] F. N. Schwettman, J. Appl. Phys. **45**, 1918 (1974).
[8] G. L. Vick and K. M. Whittle, J. Electrochem. Soc. **119**, 1142 (1969).
[9] B. S. Meyerson, in *Semiconductor Silicon*, edited by G. Harbeke and M. J. Schulz, Springer Series in Materials Science Vol. 13 (Springer-Verlag, New York, 1988), p. 24.
[10] C. P. Parry, R. A. Kubiak, S. M. Newstead, T. E. Whall, and E. H. C. Parken, J. Appl. Phys. **71**, 118 (1992).
[11] S. Solmi, E. Landi, and F. Baruffaldi, J. Appl. Phys. **68**, 3250 (1990).
[12] P. Hirsch, A. Howie, R. Nicholson, D. W. Pashley, and M. J. Whelan, *Electron Microscopy of Thin Crystals* (Krieger, Malabar, FL, 1977), p. 263.
[13] P. A. Stolk, H. J. Gossmann, D. J. Eaglesham, and J. M. Poate, Nucl. Instrum. Methods Phys. Res. B **96**, 187 (1995); S. Takeda, Jpn. J. Appl. Phys., Part 2 **30**, L639 (1991).
[14] W. Wijaranakula, J. Appl. Phys. **74**, 3783 (1993).
[15] R. C. Newman and R. S. Smith, Phys. Lett. **24A**, 671 (1967).
[16] J. Yamauchi, N. Aoki, and I. Mizushima, Phys. Rev. B **55**, R10 245 (1997).
[17] M. R. Sardela Jr., H. H. Radamson, J. O. Ekberg, J.-E. Sundgren, and G. V. Hansson, Semicond. Sci. Technol. **9**, 1272 (1994); M. R. Sardela Jr., W.-X. Ni, J. O. Ekberg, J.-E. Sundgren, and G. V. Hansson, in *Silicon Molecular Beam Epitaxy*, edited by J. C. Bean, S. Iyer, and K. Wang, MRS Symposia Proceeding No. 220 Materials Research Society, Pittsburgh, (1991), p. 109.
[18] J. Zhu, T. D. de la Rubia, L. H. Yang, C. Mailhiot, and G. H. Gilmer, Phys. Rev. B **54**, 4741 (1996); Appl. Phys. Lett. **74**, 3657 (1999).
[19] Q. Lu, T. R. Bramblett, N.-E. Lee, M.-A. Hasan, T. Karasawa, and J. E. Greene, J. Appl. Phys. **77**, 3067 (1995).
[20] D. Lubben, R. Tsu, T. R. Bramblett, and J. E. Greene, J. Vac. Sci. Technol. A **9**, 3003 (1991).
[21] H. Kim, G. Glass, S. Y. Park, T. Spila, N. Taylor, J. R. Abelson, and J. E. Greene, Appl. Phys. Lett. **69**, 3869 (1996).
[22] G. Glass, H. Kim, M. R. Sardela, Q. Lu, J. R. A. Carlsson, J. R. Abelson, and J. E. Greene, Surf. Sci. **392**, L63 (1997).
[23] H. Kim, G. Glass, T. Spila, N. Taylor, S. Y. Park, J. R. Abelson, and J. E. Greene, J. Appl. Phys. **82**, 2288 (1997).
[24] J. P. Noel, J. E. Greene, N. L. Rowell, S. Kechang, and D. C. Houghton, Appl. Phys. Lett. **55**, 1525 (1989); X. J. Zhang, G. Xue, A. Agarwal, R. Tsu, M. A. Hasan, J. E. Greene, and A. Rockett, J. Vac. Sci. Technol. A **11**, 2553 (1993).
[25] P. Desjardins and J. E. Greene, J. Appl. Phys. **79**, 1423 (1996).
[26] L. J. van der Pauw, Philips Res. Rep. **13**, 1 (1958).
[27] B. G. Streetman, *Solid State Electronic Devices*, 3rd ed. (Prentice Hall, Englewood Cliffs, NJ, 1990).
[28] M. A. Shibib and F. A Lindholm, IEEE Trans. Electron Devices **ED-27**, 1304 (1980).
[29] P. P. Debye and T. Kohane, Phys. Rev. **94**, 724 (1954).
[30] F. J. Morin and J. P. Maita, Phys. Rev. **96**, 28 (1954).
[31] J. Messier and J. M. Flores, J. Phys. Chem. Solids **24**, 1539 (1963).
[32] L. C. Linares and S. S. Li, J. Electrochem. Soc. **128**, 601 (1981).
[33] J. F. Lin, S. S. Li, L. C. Linares, and K. W. Teng, Solid-State Electron. **24**, 827 (1981).
[34] Q. Lu, M. R. Sardela, Jr., T. R. Bramblett, and J. E. Greene, J. Appl. Phys. **80**, 4458 (1996).
[35] N. F. Mott and W. D. Twose, Adv. Phys. **10**, 107 (1961).
[36] D. S. Lee and J. G. Fossum, IEEE Trans. Electron Devices **ED-30**, 626 (1983).
[37] N. F. Mott, Philos. Mag. **26**, 1015 (1972); Phys. Rev. B **44**, 265 (1981).
[38] N. F. Mott and M. Kaveh, J. Phys. C **14**, L177 (1981).
[39] H. S. Bennett, J. Appl. Phys. **59**, 2837 (1986).
[40] M. Lax and J. C. Phillips, Phys. Rev. **110**, 41 (1958).
[41] H. Frisch and S. Lloyd, Phys. Rev. **120**, 1175 (1960).
[42] J. R. Klauder, Ann. Phys. (N.Y.) **14**, 43 (1961). The third-level approximation is used here.
[43] G. D. Mahan, J. Appl. Phys. **51**, 2634 (1980).
[44] P. A. Sterne and J. C. Inkson, J. Appl. Phys. **52**, 6432 (1981).
[45] S. Wagner, J. Electrochem. Soc. **119**, 1570 (1972).
[46] G. A. Slack and M. A. Hussain, J. Appl. Phys. **70**, 2694 (1991).
[47] W. R. Thurber, R. L. Mattis, Y. M. Liu, and J. J. Filliben, J. Electrochem. Soc. **127**, 2291 (1980).
[48] D. Caughy and R. Thomas, Proc. IEEE **55**, 2192 (1967).
[49] M. A. G. Halliwell, M. H. Lyons, S. T. Davey, M. Hockley, C. G. Tuppen, and C. J. Gibbings, Semicond. Sci. Technol. **4**, 10 (1989); F. Bozso and Ph. Avouris, Phys. Rev. B **38**, 3943 (1988).
[50] D. Taupin, Bull. Soc. Fr. Mineral. Cristallogr. **87**, 469 (1964).
[51] S. Takagi, J. Phys. Soc. Jpn. **26**, 1239 (1969).
[52] S. A. Barnett and J. E. Greene, Surf. Sci. **151**, 67 (1985).
[53] P. Fewster, Semicond. Sci. Technol. **8**, 1915 (1993).
[54] P. Fewster, J. Appl. Crystallogr. **22**, 64 (1989).
[55] D. D. Perovic, G. C. Weatherly, R. F. Egerton, D. C. Houghton, and T. E. Jackman, Philos. Mag. A **63**, 757 (1991).
[56] H. Gao and W. Nix, Annu. Rev. Mater. Sci. **29**, 173 (1999).
[57] P. A. Stolk, H.-J. Gossman, D. J. Eaglesham, and J. M. Poate, Mater. Sci. Eng., B **36**, 275 (1996); M. D. Johnson, M. J. Caturla, and T. D. de la Rubia, J. Appl. Phys. **84**, 1963 (1998).
[58] Reported equilibrium solid solubilities at 900 °C are $6\times10^{20}$ $cm^{-3}$ for P, $3\times10^{19}$ $cm^{-3}$ for Sb, $2\times10^{19}$ $cm^{-3}$ for Ga, and $1.5\times10^{19}$ $cm^{-3}$ for Al. For B in Si, reported solid solubilties range from $2\times10^{19}$ $cm^{-3}$ at 700 °C to $8\times10^{20}$ $cm^{-3}$ at 1400 °C. See *Impurities and Defects in Group IV Elements and III-V Compounds*, edited by O. Madelung and M. Schulz, Landolt-Börnstein, New Series, Group III, Vol. 22, Pt. a (Springer, Berlin, 1989).
[59] P. Ostoja, D. Nobili, A. Armigliato, and R. Angelucci, J. Electrochem. Soc. **123**, 124 (1976).
[60] *Handbook of Chemistry and Physics*, 77th ed., edited by D. R. Lide (CRC Press, Boca Raton, FL, 1996).
[61] B. E. Weir, R. L. Headrick, Q. Shen, L. C. Feldman, M. S. Hybertsen, M. Needels, M. Schluter, and T. R. Hart, Phys. Rev. B **46**, 12 861 (1992).
[62] E. Tarnow, J. Phys.: Condens. Matter **4**, 5405 (1992).
[63] W. Luo, P. B. Rasband, P. Clancy, and B. W. Roberts, J. Appl. Phys. **84**, 2476 (1998).
[64] A. Vailionis, G. Glass, P. Desjardins, David G. Cahill, and J. E. Greene, Phys. Rev. Lett. **82**, 4464 (1999).
[65] T. R. Bramblett, Q. Lu, T. Karasawa, M.-A. Hasan, S. K. Jo, and J. E. Greene, J. Appl. Phys. **76**, 1884 (1994).
[66] J. R. Engstrom, L. Q. Xia, M. J. Furjanic, and D. A. Hansen, Appl. Phys. Lett. **63**, 1821 (1993).
[67] J. E. Vasek, Z. Zhang, C. T. Salling, and M. G. Lagally, Phys. Rev. B **51**, 17 207 (1995); S. Jeong and A. Oshiyama, *ibid.* **58**, 12 958 (1998); J. Nara, T. Sasaki, and T. Ohno, Appl. Surf. Sci. **130-132**, 254 (1998).